



# Type Ib Supernova Master OT J120451.50+265946.6: Radio-emitting Shock with Inhomogeneities Crossing through a Dense Shell

Poonam Chandra<sup>1,2</sup>, A. J. Nayana<sup>1</sup>, C.-I. Björnsson<sup>2</sup>, Francesco Taddia<sup>2</sup>, Peter Lundqvist<sup>2</sup>, Alak K. Ray<sup>3</sup>, and Benjamin J. Shappee<sup>4</sup>

<sup>1</sup> National Centre for Radio Astrophysics, Tata Institute of Fundamental Research, P.O. Box 3, Pune, 411007, India; [poonam@ncra.tifr.res.in](mailto:poonam@ncra.tifr.res.in)

<sup>2</sup> Department of Astronomy, Stockholm University, AlbaNova, SE-106 91 Stockholm, Sweden

<sup>3</sup> Homi Bhabha Centre for Science Education, Tata Institute of Fundamental Research, Mankhurd, Mumbai, 400088, India

<sup>4</sup> Institute for Astronomy, University of Hawai'i, 2680 Woodlawn Drive, Honolulu, HI 96822, USA

Received 2018 April 27; revised 2019 April 11; accepted 2019 April 12; published 2019 May 28

## Abstract

We present radio observations of Type Ib supernova (SN) Master OT J120451.50+265946.6. Our low-frequency Giant Metrewave Radio Telescope (GMRT) data, taken when the SN was in the optically thick phase for observed frequencies, reveal inhomogeneities in the structure of the radio-emitting region. The high-frequency Karl G. Jansky Very Large Array data indicate that the shock is crossing through a dense shell between  $\sim 47$  and  $\sim 87$  days. The data  $\geq 100$  days onward are reasonably well fit with the inhomogeneous synchrotron self-absorption model. Our model predicts that the inhomogeneities should smooth out at late times. Low-frequency GMRT observations at late epochs will test this prediction. Our findings suggest the importance of obtaining well-sampled wide-band radio data in order to understand the intricate nature of the radio emission from young supernovae.

*Key words:* circumstellar matter – radiation mechanisms: non-thermal – radio continuum: general – supernovae: general – supernovae: individual (Master OT J120451.50+265946.6)

## 1. Introduction

Core-collapse supernovae (SNe) are energetic explosions that mark the death of massive stars with masses  $M > 8M_{\odot}$ . SNe Ib/c are characterized by the absence of H and/or He lines in their optical spectra, suggesting that the outer H/He envelopes of the progenitor star were ejected before the explosion in these SNe (Woosley et al. 2002). These are collectively called stripped-envelope SNe (Clocchiatti & Wheeler 1997). Among all local SNe (distance  $d < 60$  Mpc), 19% belong to the class of SNe Ib/c (Li et al. 2011).

The proposed plausible progenitors of SNe Ib/c are Wolf-Rayet (W-R) stars that strip most of their outer envelope(s) via strong stellar winds and stars in close binary systems where H/He envelopes of the progenitor star are stripped via binary interactions (Ensmann & Woosley 1988). The physical mechanisms by which the progenitors of SNe Ib/c lose their H/He envelopes before the explosion and the timescales involved in this process remain open questions.

The progenitor systems of SNe Ib/c are poorly constrained from direct detection efforts from preexplosion images (Smartt 2009). However, independent constraints on the properties of SN progenitors can be obtained by studying the interaction of SNe with their circumstellar medium (CSM), formed due to mass lost from the progenitor systems during their evolutionary phases. The mass loss during the evolution can be constant, creating steady stellar winds, or can occur via episodic events (Dopita et al. 1984), creating a complex density field around the star. Radio emission, emitted via the synchrotron mechanism, is one of the best signatures to study the SN ejecta interaction with the CSM and probes the properties of the CSM (Chevalier 1982a).

In this work, we report the radio observations of SN Master OT J120451.50+265946.6 (hereafter SN J1204). SN J1204 was discovered on 2014 October 28.87 (UT) by Gress et al. (2014) with an optical magnitude  $m_v = 13.9$  and at

a position  $\alpha_{J2000} = 12^{\text{h}}04^{\text{m}}51^{\text{s}}.5$ ,  $\delta_{J2000} = +26^{\circ}59'46''.6$ . The SN exploded in galaxy NGC 4080 at a distance  $d \sim 15$  Mpc (Karachentsev & Kaisina 2013). SN J1204 was classified as a type Ib SN based on the spectrum obtained with the 2 m Himalayan Chandra Telescope (HCT) of the Indian Astronomical Observatory on 2014 October 29.0 UT (Srivastav et al. 2014). Later Terreran et al. (2014) confirmed the classification using the spectrum obtained with the Asiago 1.82 m telescope. The expansion velocity was found to be  $8300 \text{ km s}^{-1}$  from the He II absorption feature in the HCT spectrum (Srivastav et al. 2014). SN J1204 observations with the X-ray telescope (XRT) on-board *Swift* during 2014 October 29–November 04 yielded upper limits (Margutti et al. 2014).

The radio emission from SN J1204 was first detected at 5 GHz with the Karl G. Jansky Very Large Array (VLA) on 2014 October 31.5 with a flux density of  $3.00 \pm 0.02$  mJy (Kamble et al. 2014). The Giant Metrewave Radio Telescope (GMRT) detected the radio emission at the SN position at 1390 MHz with a flux density of 1.56 mJy on 2014 November 26.09 UT (Chandra et al. 2014). In this paper, we present the results of an extensive radio follow-up of SN J1204 with the GMRT, combined with the publicly available data with the VLA. Thus, covering a frequency range of 0.33–24 GHz for more than 1000 days since discovery, we carry out detailed spectral and temporal modeling of the SN and derive the nature of the radio emission.

The paper is organized as follows. In Section 2, we summarize the observations at various wavebands and procedures for data analysis. We use the optical photometry data to best constrain the epoch of explosion in Section 3. In Section 4, we attempt to fit the data with the standard models of radio emission and show that this model is incapable of fitting the data. We develop and fit an inhomogeneous model to the radio data in Section 5. In addition, in this section, we also discuss the presence of a dense shell. Finally, we discuss our results, compare the properties of SN J1204 with other

**Table 1**  
Details of GMRT Observations of SN Master OT J120451.50+265946.6 (SN J1204)

Date of Observation (UT)	Age <sup>a</sup> (day)	Frequency (GHz)	Flux Density		Map rms ( $\mu\text{Jy beam}^{-1}$ )	Resolution ( $'' \times ''$ )
			SN (mJy)	Test Source <sup>b</sup> (mJy)		
2014 Nov 26.1	61.1	1.39	$1.54 \pm 0.17$	$6.99 \pm 0.70$	41	$2.30 \times 1.95$
2014 Dec 14.0	79.0	1.39	$1.63 \pm 0.18$	$6.40 \pm 0.65$	44	$2.28 \times 1.96$
2015 Jan 29.8	125.8	1.39	$3.18 \pm 0.33$	$5.85 \pm 0.59$	50	$3.88 \times 2.03$
2015 May 30.4	246.4	1.39	$1.65 \pm 0.19$	$6.09 \pm 0.62$	62	$3.65 \times 2.73$
2015 Jul 04.4	281.4	1.39	$1.33 \pm 0.17$	$6.37 \pm 0.64$	46	$2.24 \times 1.84$
2015 Jul 17.5	294.5	1.39	$1.14 \pm 0.13$	$6.28 \pm 0.63$	40	$2.20 \times 2.01$
2015 Aug 17.5	325.5	1.39	$0.90 \pm 0.11$	$5.85 \pm 0.59$	44	$2.59 \times 2.06$
2015 Aug 21.6	326.6	1.39	$1.01 \pm 0.15$	$5.64 \pm 0.58$	60	$3.88 \times 2.02$
2015 Sep 18.5	357.5	1.39	$0.85 \pm 0.17$	$6.96 \pm 0.72$	80	$8.58 \times 3.06$
2017 Apr 21.6	938.6	1.39	$0.22 \pm 0.06$	$5.31 \pm 0.54$	40	$3.88 \times 2.02$
2014 Dec 03.0	68.0	0.61	$0.47 \pm 0.12$	$13.14 \pm 1.32$	68	$5.14 \times 4.18$
2014 Dec 21.9	86.9	0.61	$0.53 \pm 0.11$	$15.91 \pm 1.60$	60	$6.60 \times 4.30$
2015 Feb 03.1	130.1	0.61	$1.00 \pm 0.18$	$15.78 \pm 1.58$	59	$9.03 \times 4.74$
2015 Mar 14.8	169.8	0.61	$1.56 \pm 0.19$	$15.29 \pm 1.53$	55	$5.00 \times 4.22$
2015 May 01.6	217.6	0.61	$1.98 \pm 0.25$	$16.37 \pm 1.65$	78	$5.76 \times 4.30$
2015 Jun 06.4	253.4	0.61	$2.48 \pm 0.28$	$17.38 \pm 1.74$	76	$6.34 \times 4.60$
2015 Jul 10.7	287.7	0.61	$2.21 \pm 0.37$	$13.86 \pm 1.40$	98	$4.48 \times 3.76$
2015 Jul 26.8	303.8	0.61	$2.26 \pm 0.27$	$15.75 \pm 1.58$	84	$5.50 \times 4.45$
2015 Sep 25.3	364.3	0.61	$1.92 \pm 0.23$	$15.94 \pm 1.60$	67	$6.20 \times 4.70$
2017 Apr 29.6	946.6	0.61	$0.57 \pm 0.11$	$16.41 \pm 1.64$	64	$6.91 \times 4.43$
2015 Jul 13.5	290.5	0.33	$\leq 1.086$	$23.13 \pm 3.49$	362	$9.33 \times 8.91$
2015 Sep 21.3	360.3	0.33	$\leq 3.87$	$22.89 \pm 3.69$	1290	$11.17 \times 7.65$
2016 Oct 21.0	756.0	0.33	$1.85 \pm 0.45$	$25.10 \pm 3.79$	245	$16.42 \times 8.47$
2017 Apr 27.5	944.5	0.33	$0.72 \pm 0.31$	$30.06 \pm 4.53$	263	$12.03 \times 8.17$
2017 Nov 27.0	1158.0	0.33	$0.89 \pm 0.38$	$29.65 \pm 4.47$	248	$11.58 \times 8.00$

**Notes.** The tabulated uncertainties in all flux density measurements are obtained using the AIPS task JMFIT plus 10% uncertainties added in quadrature for the 1390 and 610 MHz bands and 15% for the 325 MHz band.

<sup>a</sup> The age is calculated assuming 2014 September 26 (UT) as the date of explosion (see Section 3).

<sup>b</sup> Nearby constant flux density test source at a position of  $\alpha_{J2000} = 12^{\text{h}}04^{\text{m}}29^{\text{s}}.01$ ,  $\delta_{J2000} = +27^{\circ}03'45''.3$  (see Section 2.1.1).

stripped-envelope SNe, and summarize our main conclusions in Section 6.

## 2. Observations and Data Analysis

### 2.1. Radio Observations

SN J1204 has been extensively observed in the radio bands using the GMRT and the VLA. Below we describe the observations and procedures for data analysis.

#### 2.1.1. GMRT Observations

We started the GMRT observations of SN J1204 on 2014 November 26.09 UT and continued monitoring observations for about 3 yr. The observations covered the frequency bands of 1390, 610, and 325 MHz. The observations were carried out in total intensity mode (Stokes  $I$ ), and the data were acquired with an integration time of 16.1 s. The observed bandwidth was 33 MHz, split into 256 channels at all observed frequencies and epochs. A flux calibrator (either 3C 286 or 3C 147) was observed once during each observing run to calibrate the amplitude gains of individual antennas. Phase calibrators (J1125+261, J1227+365 or J1156+314) were observed every  $\sim 35$  minutes for  $\sim 5$  minutes throughout each observing run to correct for phase variations due to atmospheric fluctuations. The data were analyzed using the Astronomical Image Processing System (AIPS). Initial flagging and calibration

were done using the software FLAGCAL, developed for automatic flagging and calibration for the GMRT data (Prasad & Chengalur 2012). The flagged and calibrated data were closely inspected, and further flagging and calibration were done manually until the data quality looked satisfactory. The calibration solutions obtained for a single channel were applied to the full bandwidth. Instead of averaging the full bandwidth, only a few channels (20 channels for the 1390 MHz band, 15 channels for the 610 MHz band, and 7 channels for the 325 MHz band) were averaged together to avoid bandwidth smearing. Fully calibrated data of the target source were imaged using the AIPS task IMAGR. A few rounds of phase self-calibration and one round of amplitude plus phase (a&p) self-calibration were performed. During the a&p self-calibration, the voltage gains were normalized to unity to minimize the drifting of the flux-density scale. In addition, the flux densities of SN J1204 and the test source were measured between the a&p and the last phase self-calibration rounds, and they were found to be consistent. The flux density of the SN was measured by fitting a Gaussian at the SN position using the AIPS task JMFIT. This is a standard procedure followed for the GMRT data analysis (e.g., Chandra & Kanekar 2017, and references therein). The data on 2015 April 25 were found to be corrupted, and we did not use them for further analysis. The details of GMRT observations and the SN flux densities are summarized in Table 1.

To estimate whether there is a contribution from the host galaxy at the SN position, in Figure 1 we plot the the contour map for the SN field. We do not find any contamination by the host galaxy at the SN position within  $3\sigma$  noise.

To confirm that the variability seen in the SN flux density at various epochs is real, we chose a nearby nonvariable test source NVSS J120428+270343 at a position of  $\alpha_{J2000} = 12^{\text{h}}04^{\text{m}}29^{\text{s}}.01$ ,  $\delta_{J2000} = +27^{\circ}03'45''.3$ . The source was selected such that its flux density was found to be constant within the uncertainties of 10% of the source flux between the NVSS (Condon et al. 1998) and the FIRST (White et al. 1997; Helfand et al. 2015) surveys. The flux density of the test source in our observations is constant within  $\sim 10\%$  errors at 1390 and 610 MHz bands and within  $\sim 15\%$  at the 325 MHz band at various epochs (Table 1). This is roughly consistent with the uncertainties in the GMRT data due to systematic errors (Chandra & Kanekar 2017). Thus for fitting the data, we add 10% uncertainty in quadrature at 1390 and 610 MHz bands and 15% at 325 MHz bands.

### 2.1.2. VLA Observations

We analyzed the publicly available archival VLA data for SN J1204 at five epochs from 2014 October 31 to 2015 July 31 spanning a frequency range of 1–24 GHz. The data had bandwidth of  $\approx 1$  GHz split into eight spectral windows at 1.515 GHz and  $\approx 2$  GHz split into 16 spectral windows for all other frequencies. We carried out the VLA data analysis using standard packages within the Common Astronomy Software Applications package (CASA, McMullin et al. 2007). The CASA task “clean” was used to make images of the data. The details of the VLA observations, array configurations, and flux densities of the SN are summarized in Table 2. We add 5% error in the quadrature for the VLA data, a typical uncertainty in the flux density calibration scale at the observed frequencies.<sup>5</sup>

### 2.2. Optical Observations

We used the data from All-Sky Automated Survey for Supernovae (ASAS-SN; Shappee et al. 2014) in *V*-magnitude band, covering the preexplosion phase up to 400 days before the assumed explosion date until 1200 days postexplosion. ASAS-SN images were processed by a fully automatic ASAS-SN pipeline using the Interactive Spectral Interpretation System (Houck & Denicola 2000) image subtraction package (Alard & Lupton 1998; Alard 2000). For this the stacking was done on the three dithered images before carrying out the photometry. For the subtraction, the stacked images were subtracted from a good reference image. We performed aperture photometry on the subtracted images using the Image Reduction and Analysis Facility (Tody 1986, 1993) “apphot” package and calibrated the results using the AAVSO photometric All-Sky Survey (Henden et al. 2015). Some of the data points were found to be affected by clouds in the field of view or by the incidence of cosmic rays, and these data were discarded. The ASAS-SN detections and  $3\sigma$  limits are shown in Figure 2. SN J1204 is, unfortunately, only detected after a seasonal gap, which resulted in missing the peak of the SN light curve.

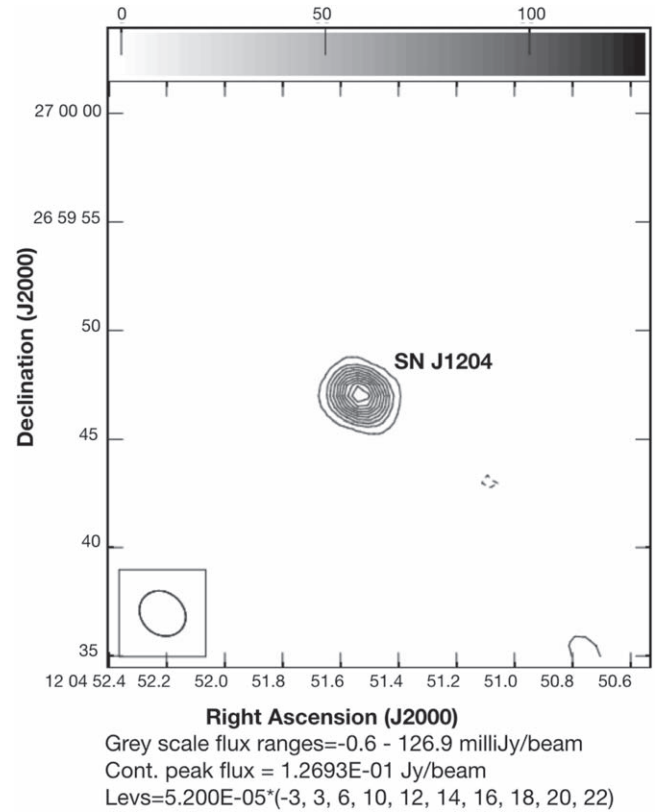


**Figure 1.** Contour plot map of the SN J1204 field at the GMRT 1387 MHz band. The contours are marked as 3, 6, 10, 12, 14, 16, 18, 20, 22 times the map uncertainty very near to the SN position. Note that there is no contaminating source at the SN position within  $3\sigma$ .

### 2.3. X-Ray Observations

SN J1204 was observed with the *Swift*-XRT covering a period almost up to 1000 days since its discovery. In addition, *Chandra* observed it for around 10 ks on 2014 November 16. We analyzed the publicly available archival data from both the telescopes (see Table 3).

For the *Chandra* data analysis, the *Chandra* Interactive Analysis of Observations software (CIAO; Fruscione et al. 2006) was used. We extracted spectra, response, and ancillary matrices using the CIAO task *specextractor*. The CIAO version 4.9 along with CALDB version 4.7.6 was used for this purpose.

The *Swift*-XRT spectra and response matrices were extracted using the online XRT products building pipeline<sup>6</sup> (Goat et al. 2007; Evans et al. 2009). We used the XRT specific tasks *XSELECT*, *XIMAGE*, and *SOSTA* of the package HEASOFT<sup>7</sup> to carry out the spectral analysis and obtained  $3\sigma$  limits on the count rates.

The SN was not detected in any of the X-ray observations. The count-rate simulator *WebPIMMS*,<sup>8</sup> using a temperature of 5 keV and Galactic absorption column density of  $N_{\text{H}} = 1.7 \times 10^{20} \text{ cm}^{-2}$  toward the SN direction (Dickey & Lockman 1990; Kalberla et al. 2005), was used to estimate the upper limits on the unabsorbed flux of the SN in Table 3. A distance of 15 Mpc was used to convert the fluxes into unabsorbed luminosities.

<sup>5</sup> <https://science.nrao.edu/facilities/vla/docs/manuals/oss/performance/fdscale>

<sup>6</sup> [http://www.swift.ac.uk/user\\_objects/](http://www.swift.ac.uk/user_objects/)

<sup>7</sup> <http://heasarc.gsfc.nasa.gov/docs/software/lheasoft/>

<sup>8</sup> <https://heasarc.gsfc.nasa.gov/cgi-bin/Tools/w3pimms/w3pimms.pl>

**Table 2**  
Details of VLA Observations of Master OT J120451.50+265946.6

Date of Observation (UT)	Age <sup>a</sup> (day)	Frequency (GHz)	VLA Array Configuration	Flux density (mJy)	rms ( $\mu\text{Jy beam}^{-1}$ )
2014 Oct 31.5	35.5	4.799	C	$2.938 \pm 0.151$	10
...	...	7.099	C	$2.213 \pm 0.117$	9
2014 Nov 12.5	47.5	1.515	C	$1.420 \pm 0.123$	80
...	...	4.799	C	$2.520 \pm 0.131$	13
...	...	7.099	C	$1.858 \pm 0.097$	12
...	...	13.499	C	$0.886 \pm 0.046$	14
...	...	15.999	C	$0.696 \pm 0.040$	18
...	...	19.199	C	$0.583 \pm 0.038$	22
...	...	24.499	C	$0.429 \pm 0.039$	27
2015 Jan 08.4	103.4	1.515	CnB	$2.404 \pm 0.142$	32
...	...	2.529	CnB	$3.238 \pm 0.165$	30
...	...	3.469	CnB	$2.707 \pm 0.137$	15
...	...	4.799	CnB	$2.151 \pm 0.109$	19
...	...	7.099	CnB	$1.495 \pm 0.076$	22
...	...	13.499	CnB	$0.781 \pm 0.041$	22
...	...	15.999	CnB	$0.622 \pm 0.032$	12
...	...	19.199	CnB	$0.495 \pm 0.036$	16
...	...	24.499	CnB	$0.367 \pm 0.030$	18
2015 Apr 22.1	207.1	1.515	B	$1.793 \pm 0.111$	14
...	...	2.529	B	$1.186 \pm 0.064$	14
...	...	3.469	B	$0.886 \pm 0.051$	13
...	...	4.799	B	$0.683 \pm 0.038$	14
...	...	7.099	B	$0.476 \pm 0.028$	13
...	...	13.499	B	$0.224 \pm 0.021$	13
...	...	15.999	B	$0.162 \pm 0.024$	13
...	...	19.199	B	$0.181 \pm 0.018$	17
...	...	24.499	B	$0.124 \pm 0.019$	21
2015 Jul 31.1	307.1	1.515	A	$1.010 \pm 0.130$	17
...	...	2.529	A	$0.500 \pm 0.036$	16
...	...	3.469	A	$0.466 \pm 0.038$	16
...	...	4.799	A	$0.452 \pm 0.032$	13
...	...	7.099	A	$0.241 \pm 0.019$	12
...	...	8.599	A	$0.193 \pm 0.017$	13
...	...	10.999	A	$0.181 \pm 0.014$	16

**Notes.** The uncertainties in the flux density measurements reflect the map uncertainty and 5% uncertainty in flux density estimation added in quadrature.

<sup>a</sup> The age is calculated using 2014 September 26 (UT) as the date of explosion.

### 3. Constraining the Explosion Epoch

There is a large uncertainty in the date of explosion for SN J1204. The HCT spectrum on 2014 October 29.0 UT best matched with several normal SNe Ib a few weeks after the maximum (Srivastav et al. 2014). Since the typical rest-frame rise time of SNe Ib is  $\sim 21$  days (Taddia et al. 2015), the explosion date is likely to be 30–50 days before the discovery.

We attempt to estimate the explosion epoch based on the optical light curves. Our data are mainly in the  $V$ -band from the ASAS-SN observations, but we also have an unfiltered magnitude point from the discovery telegram (13.9 mag at JD 2,456,959.37; Gress et al. 2014) obtained by the MASTER Global Robotic Net (Lipunov et al. 2010). The discovery magnitude was significantly brighter than the rest of the data, suggesting that the SN was discovered around the peak and that the rest of the data belong to the linear tail of the light curve. To quantify the phase of our observations with respect to the  $V$ -band peak magnitude, we compared them to the stripped-envelope SN light-curve templates from Taddia et al. (2018), in the  $V$ - as well as in the  $r$ - bands. The match between our data and the templates is shown in Figure 3. Here we considered that on average stripped-envelope SNe peak 0.124 mag brighter in the  $r$ -band than in the  $V$ -band and that the peak in the

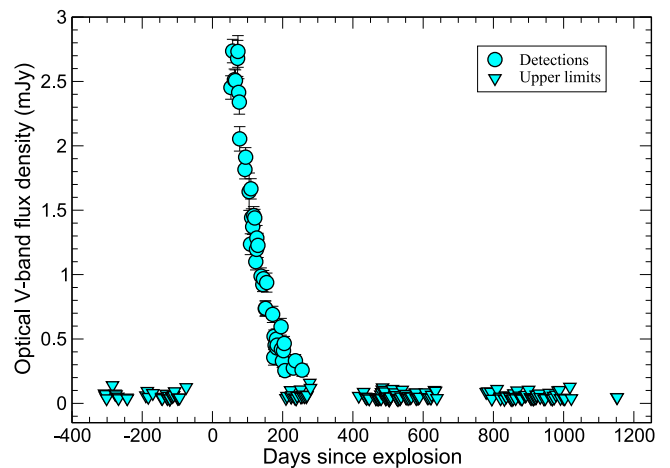


**Figure 2.** ASAS-SN optical data for SN J1204 covering epochs 400 days before the SN explosion until 1200 days postexplosion. The detections are indicated by circles, and the  $3\sigma$  upper limits are indicated by triangles. Zero time corresponds to the SN explosion date, i.e., 2014 September 26 UT.

$r$ -band occurs 1.23 days after the one in the  $V$ -band (Taddia et al. 2018). We also assumed that the open-filter magnitude from MASTER can be treated as an  $r$ -band point (see, e.g.,

**Table 3**  
X-Ray Observations of Master OT J120451.50+265946.6 (SN J1204)

Date of obsn (UT)	Age <sup>a</sup> (day)	Telescope	ObsID	Exposure (ks)	Count Rate <sup>b</sup> (counts s <sup>-1</sup> )	Flux <sup>b</sup> (erg s <sup>-1</sup> cm <sup>-2</sup> )	Luminosity <sup>b</sup> (erg s <sup>-1</sup> )
2014 Oct 29.50	33.50	Swift-XRT	00033511001	1.98	$<7.66 \times 10^{-3}$	$<2.62 \times 10^{-13}$	$<7.06 \times 10^{39}$
2014 Nov 02.83	36.83	Swift-XRT	00033511002	1.61	$<7.05 \times 10^{-3}$	$<2.41 \times 10^{-13}$	$<6.49 \times 10^{39}$
2014 Nov 04.30	38.30	Swift-XRT	00033511003	1.61	$<7.05 \times 10^{-3}$	$<2.41 \times 10^{-13}$	$<6.49 \times 10^{39}$
2014 Nov 16.88	50.88	Chandra-ACIS	16006	9.65	$<2.36 \times 10^{-4}$	$<8.06 \times 10^{-15}$	$<2.17 \times 10^{38}$
2015 Nov 25.74	424.74	Swift-XRT	00084388001	4.59	$<2.46 \times 10^{-3}$	$<8.41 \times 10^{-14}$	$<2.27 \times 10^{39}$
2017 Jan 21.83	847.83	Swift-XRT	00033511001	1.65	$<7.01 \times 10^{-3}$	$<2.40 \times 10^{-13}$	$<6.46 \times 10^{39}$
2017 Oct 29.69	1128.69	Swift-XRT	00084388002	0.55	$<2.11 \times 10^{-2}$	$<7.21 \times 10^{-13}$	$<1.94 \times 10^{40}$

#### Notes.

<sup>a</sup> The age is calculated using 2014 September 26 (UT) as the date of explosion.

<sup>b</sup> The values are in the energy range 0.3–10 keV.

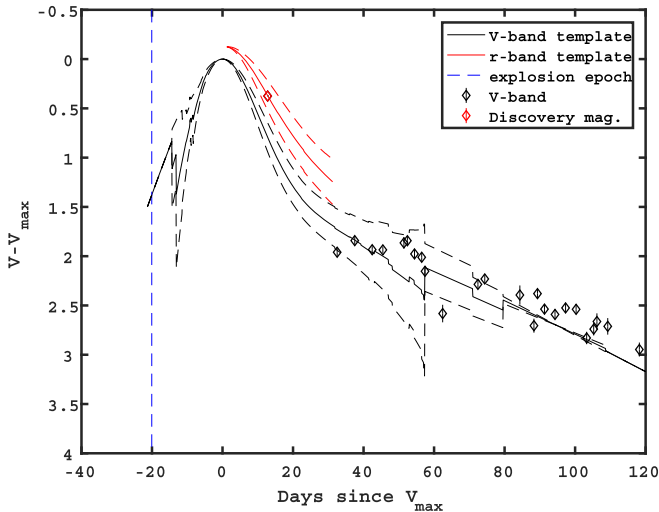


**Figure 3.** Match between optical light curves and  $V$ - and  $r$ -band templates from Taddia et al. (2018). The  $V$ -band is shown in black, and the  $r$ -band in red. The uncertainty of the templates is marked by dashed curves. The estimated explosion epoch is marked by a vertical dashed blue line and was obtained assuming a standard rise time for SNe Ib from Taddia et al. (2018).

Tsvetkov et al. 2017). Finally, we only considered the first four  $V$ -band points for the fit, which are those within 50 days since maximum, when the  $V$ -band template has a relatively small spread. From the best match between the data and the templates we derive the  $V$ -band peak epoch (JD 2,456,946.55  $\pm$  3.00). From this epoch we subtracted the average  $V$ -band rise time for SNe Ib (from Taddia et al. 2015), which is 20.07  $\pm$  1.86 days. This gives the best explosion date to be JD 2,456,926.5  $\pm$  3.5. This corresponds to UT date of 2014 September 26 within an uncertainty of 3.5 days. This error on the explosion epoch takes into account the typical light-curve shape of stripped-envelope SNe. In the unlikely case that SN J1204 is similar to SN 2005bf or 2011bm, that is, to rare stripped-envelope SNe with long rise times, our explosion epoch would have happened between 10 and 20 days earlier.

We note that for the computed  $V$ -band peak epoch, the classification spectrum (obtained on 2014 October 29th, Srivastav et al. 2014) occurred  $\sim$ 13 days after the peak, consistent with the phase indicated by them (a few weeks after maximum). Furthermore, the helium-I velocity of 8300 km s<sup>-1</sup> reported by Srivastav et al. (2014) is in line with the average helium-I velocities measured for SNe Ib at that phase after peak

(Taddia et al. 2018). Thus in this paper we assume 2014 September 26 UT as the date of explosion for SN J1204.

## 4. Modeling and Results

### 4.1. Visual Inspection of the Data

SN J1204 is one of the handful of SNe for which extensive data exist at radio frequencies. In Figure 4(A), we plot all the radio data from the 0.33 to 24.5 GHz frequency bands covering the epochs  $\sim$ 35 days until  $\sim$ 1158 days. In addition, we plot near-simultaneous spectral indices at various adjacent frequencies and various epochs in Figure 4(B).

The first look at the data reveals that the data are optically thin at frequencies higher than 2.53 GHz onwards. A significant fraction of low-frequency ( $\leq$ 1.5 GHz) data are in the optically thick phase. The first two observations at 0.33 GHz resulted in upper limits that prohibit us from constraining the absorption peak at this band; however, we are able to constrain it at the other two GMRT frequencies. The 1.39 and 0.61 GHz light curves peak on  $\sim$ 126 days (peak flux density  $\sim$ 3.2 mJy) and  $\sim$ 253 days (peak flux density  $\sim$ 2.5 mJy), respectively. The peak spectral luminosity at 1.39 GHz is  $\sim$ 8.6  $\times$  10<sup>26</sup> erg s<sup>-1</sup> Hz<sup>-1</sup>, consistent with the radio spectral luminosity of SNe Ib/c, which spans a range of  $L_\nu = 10^{25}$ –10<sup>29</sup> erg s<sup>-1</sup> Hz<sup>-1</sup> (Soderberg 2007).

### 4.2. Standard Model of Radio Emission

In an SN explosion, stellar ejecta are thrown out into the CSM at supersonic velocities, which drive a “forward” shock propagating into the CSM and a “reverse” shock moving back into the ejecta. Electrons are accelerated to relativistic energies in the forward shock via diffusive shock acceleration and produce synchrotron radiation in the presence of amplified magnetic fields. A model for the ejecta-CSM interaction and its evolution was developed by Chevalier (1982b). This model follows a self-similar solution with the shock radius evolving as a power law in time, that is,  $R \propto t^m$ , where  $m$  is the shock deceleration parameter, which is connected to the outer ejecta density profile  $n$  (in  $\rho_{ej} \propto R^{-n}$ ) as  $m = (n - 3)/(n - s)$ . Here  $s$  is the index of the unshocked CSM density profile,  $\rho_w$ , created by the stellar wind of the progenitor star ( $\rho_w \propto R^{-s}$ ). For a steady stellar wind,  $s = 2$ .

The radio emission in SNe can be initially suppressed either due to free-free absorption (FFA) by the ionized CSM (Chevalier 1982b) or/and due to synchrotron self-absorption

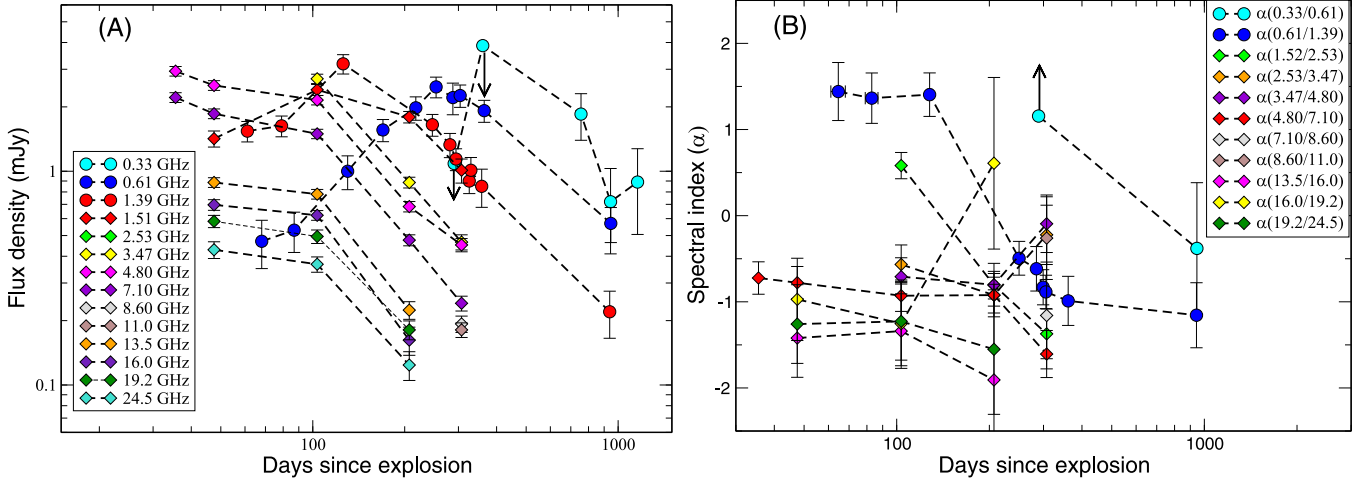


**Figure 4.** Light curves of SN J1204 at frequencies 0.610, 1.4, 2.529, 3.469, 4.799, 7.099, 13.499, 15.999, 19.199, and 24.499 GHz are plotted in the left panel (A). All GMRT data points are represented using circle symbols, and all VLA data points are represented using diamond symbols. The *L*-band data ( $\sim 1.4$  GHz) denoted in red include both 1.39 GHz GMRT measurements (circles) and 1.515 GHz VLA measurements (diamonds). We plot the near-simultaneous spectral indices between adjacent frequencies at various epochs in the right panel (B).

(SSA) by the same electron population responsible for the radio emission (Chevalier 1998). These processes can be distinguished via their early radio light curves and spectra in the optically thick phase. As the shell expands, the optical depth decreases, and at optical depth unity SNe spectra show transition from an optically thick to optically thin regime indicated by a change in the sign of the spectral index. Observations spanning over this transition are critically important to pin down the dominant absorption processes, which give information about the magnetic field, size of the emitting object, density, mass-loss rates, and so on.

Even though SNe Ib/c generally have SSA as the dominant absorption mechanism, we start our modeling considering both FFA and SSA mechanisms.

In a model where FFA is the dominant absorption mechanism, the radio flux density,  $F(\nu, t)$ , can be expressed as (Weiler et al. 2002)

$$F(\nu, t) = K_1 \left( \frac{\nu}{1 \text{ GHz}} \right)^{-\alpha} \left( \frac{t}{100 \text{ days}} \right)^{-\beta} e^{-\tau_{\text{ffa}}(\nu, t)}, \quad (1)$$

where  $K_1$  is a normalization factor whose value will be equal to the radio flux density at 1 GHz measured on day 100 after the explosion. The parameters  $\alpha$  and  $\beta$  denote the spectral and temporal indices, respectively, in the optically thin phase. The radio spectral index  $\alpha$  can be related to the electron energy index  $p$  (in  $N(E) \propto E^{-p}$ ) as  $\alpha = (p - 1)/2$ . Here  $\tau_{\text{ffa}}$  is the optical depth characterized by the FFA due to the ionized CSM external to the emitting material, and can be written as

$$\tau_{\text{ffa}}(\nu, t) = K_2 \left( \frac{\nu}{1 \text{ GHz}} \right)^{-2.1} \left( \frac{t}{100 \text{ days}} \right)^{-\delta}, \quad (2)$$

where  $K_2$  denotes the free-free optical depth at 1 GHz measured on day 100 after the explosion. As the blast wave expands, the optical depth decreases with time as  $t^{-\delta}$ , where the index of optical depth evolution  $\delta$  is related to the shock deceleration parameter  $m$  as  $m = \delta/3$ .

For the SSA-dominated synchrotron emission from SNe, the radio flux density can be written as (Chevalier 1998)

$$F(\nu, t) = K_1 \left( \frac{\nu}{1 \text{ GHz}} \right)^{2.5} \left( \frac{t}{100 \text{ days}} \right)^{\beta'} (1 - e^{-\tau_{\text{ssa}}(\nu, t)}), \quad (3)$$

where the optical depth is characterized by SSA due to the relativistic electrons at the forward shock. The SSA optical depth  $\tau_{\text{ssa}}$  is given by

$$\tau_{\text{ssa}}(\nu, t) = K_2 \left( \frac{\nu}{1 \text{ GHz}} \right)^{-(\alpha+2.5)} \left( \frac{t}{100 \text{ days}} \right)^{-(\beta'+\beta)}, \quad (4)$$

where  $K_1$  and  $K_2$  are the flux density and optical depth normalization factors similar to the case of FFA. The flux density in the optically thick and thin phases evolves as  $\nu^{2.5}$  and  $\nu^{-\alpha}$ , respectively. Here spectral index  $\alpha$  is related to electron energy index  $p$  as  $\alpha = (p - 1)/2$ . Similar to the FFA model,  $t^{-\beta}$  is the time evolution of flux density in the optically thin phase, whereas  $t^{\beta'}$  is the flux density evolution with time in the optically thick phase. While  $\beta'$  depends on the shock deceleration parameter  $m$ ,  $\beta$  depends on  $m$  as well as electron energy index  $p$ . The exact form depends on the scalings of the magnetic field,  $B$ , and the electron energy density (Chevalier 1996). For example, if magnetic energy density and relativistic electron energy density scale with postshock energy density (model 1 of Chevalier 1996), then an optically thick light curve  $F_\nu(t) \propto R^2 B^{-1/2}$  will lead to  $\beta' = 2m + 0.5$  and then  $\beta = (p + 5 - 6m)/2$ . This involves an assumption that the magnetic field was built up by turbulent motions. However, if compression of the CSM magnetic field determines the relevant magnetic field scaling and relativistic electron energy density scales with the flux of particles into the shock front, then  $\beta' = 5m/2$  and  $\beta = (p - 1)m/2$  (model 4 of Chevalier 1996). When there are substantial data in the optically thick phase, the parameters  $\beta'$ ,  $\beta$ , and  $p$  can be independently obtained, and one can determine the relevant scalings in a particular case.

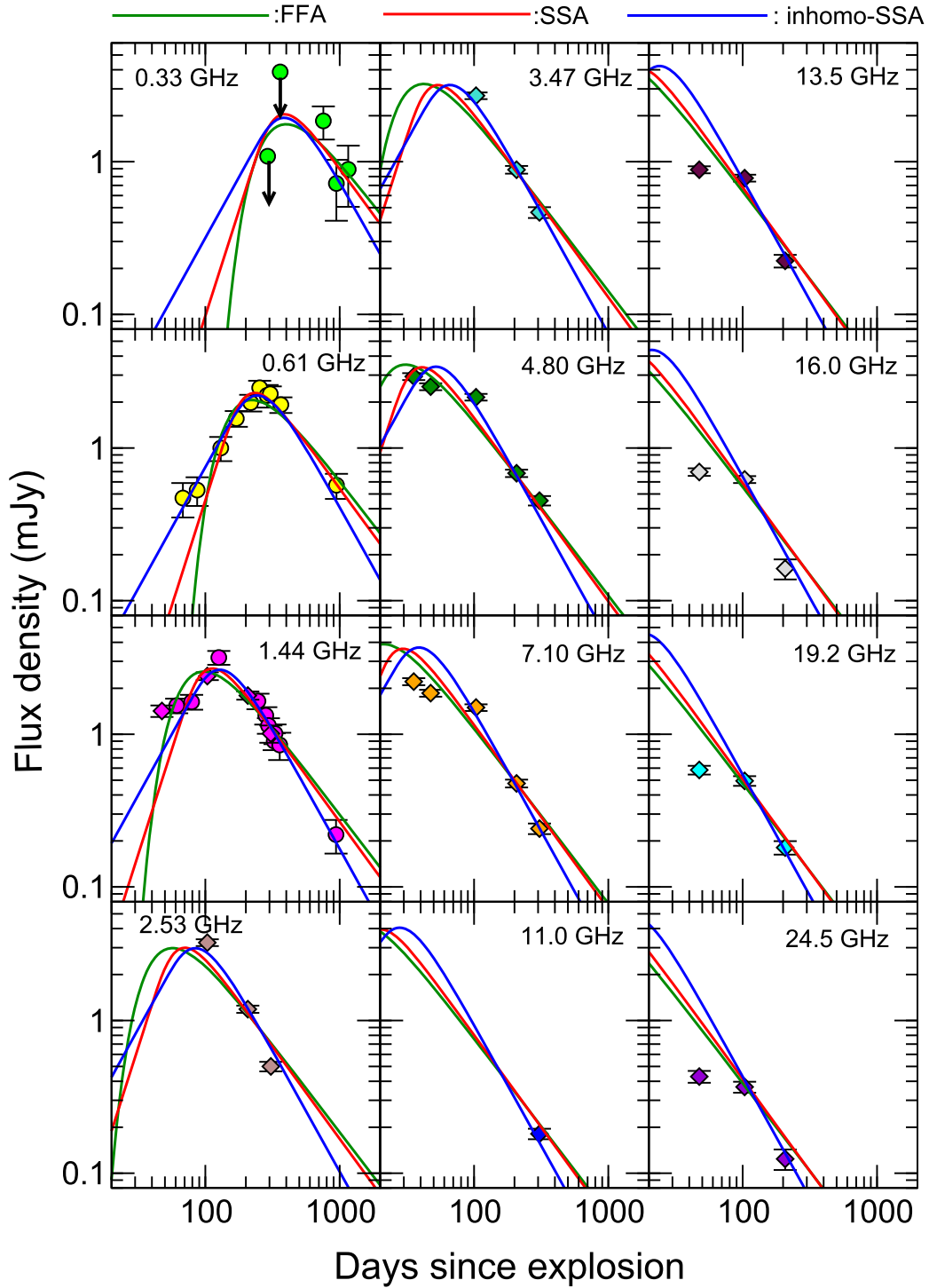


**Figure 5.** FFA and SSA model fits to the radio light curves of SN J1204 at various radio frequencies. The  $L$ -band data ( $\sim 1.4$  GHz) include both 1.39 GHz GMRT measurements (circles) and 1.515 GHz VLA measurements (diamonds). All GMRT data points are represented using a circle symbol, and all VLA data points are represented using a diamond symbol. The green line indicates FFA fits, and the red line indicate SSA fits. The blue solid lines are the best-fit curves for the inhomogeneous SSA model.

We now model the full data using both the FFA and the SSA models. We first perform the FFA model fit keeping  $K_1$ ,  $K_2$ ,  $\alpha$ ,  $\beta$ , and  $\delta$  as free parameters. The best-fit parameters are obtained using the  $\chi^2$  minimization. The fitted models along with the measured spectra and light curves are shown in Figures 5 and 6. The best-fit parameters are given in the Table 4. We note that

the reduced chi-square ( $\chi^2_\nu$ ) for the FFA model is quite high ( $\chi^2_\nu = 8.45$ ), suggesting that the FFA model is not a good fit to the radio data.

We now fit the data with the SSA model as given in Equations (3) and (4). The best-fit parameters for the SSA model are given in Table 4 and plotted in Figures 5 and 6. The

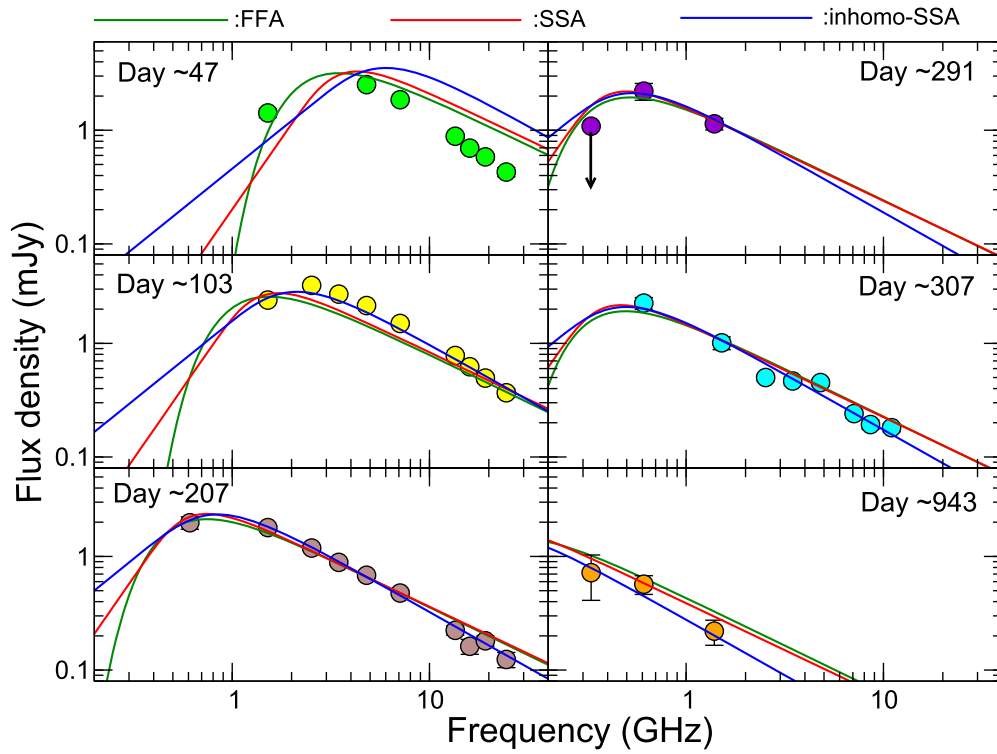


**Figure 6.** Standard FFA and SSA fits to the near simultaneous radio spectra of SN J1204 at various epochs postexplosion. The model is fitted with the complete data set including both Jansky VLA and GMRT data. The green line indicates FFA fits, and the red line indicate SSA fits. The blue solid lines are the best-fit curves for the inhomogeneous SSA model.

**Table 4**  
Best-fit Parameters Values for the Various Models to the Radio Data

FFA (full data) (1)	SSA (full data) (2)	SSA (610 MHz) (3)	SSA-inhomo (full data) (4)	SSA-inhomo ( $t > 87$ days) (5)
$K_1 = 5.75 \pm 0.95$	$K_1 = 1.56 \pm 0.29$	$K_1 = 0.70 \pm 0.04$	$K_1 = 1.50 \pm 0.14$	$K_1 = 1.45 \pm 0.13$
$K_2 = 1.07 \pm 0.21$	$K_2 = 3.72 \pm 1.06$	$K_2 = 28.55 \pm 5.90$	$K_2 = 6.56 \pm 1.41$	$K_2 = 8.00 \pm 1.00$
$\alpha = 0.84 \pm 0.12$	$\beta' = 2.76 \pm 0.27$	$\beta' = 1.49 \pm 0.12$	$\beta' = 1.59 \pm 0.12$	$\beta' = 1.56 \pm 0.21$
$\beta = 1.15 \pm 0.08$	$\beta = 1.21 \pm 0.09$	$\beta = 1.59 \pm 0.12$	$\beta = 1.59 \pm 0.10$	$\beta = 1.72 \pm 0.05$
$\delta = 2.20 \pm 0.24$	$p = 2.65 \pm 0.20$	...	$p = 2.98 \pm 0.18$	$p = 3.04 \pm 0.05$
$\chi_\mu^2 = 8.45$	$\chi_\mu^2 = 7.73$	$\chi_\mu^2 = 0.96$	$\chi_\mu^2 = 4.36$	$\chi_\mu^2 = 1.62$
dof = 52	dof = 52	dof = 6	dof = 52	dof = 39

**Note.** Here the parameters are described in Sections 4.2 and 5.1.  $\chi_\mu^2$  is the reduced chi-square, and dof is the degrees of freedom. The SSA model assumes model 1 of Chevalier (1996) with the magnetic energy density and relativistic electron energy density scale with the postshock energy density.

reduced chi-square in this case is  $\chi_\mu^2 = 7.73$ . While the SSA model performs slightly better than the FFA model, it fails to provide an acceptable fit to the data.

### 5. A Need for a Nonstandard Model

Unfortunately neither the FFA nor the SSA models provide a good fit to the radio data of SN J1204. Visual inspection of Figures 5 and 6 suggests that the data  $\leq 103$  days are not fit well with the standard models. The model overpredicts the flux on  $\sim 47$  days and underpredicts the flux at  $\sim 103$  days. The low-frequency light curves show flattening at the early epochs in the optically thick phase. The discrepancies between data and models are more pronounced at earlier epochs.

To understand the early time behavior of the radio data, we investigate the estimated spectral indices in the optically thick phase, which are mainly at the GMRT frequencies. We plot them in Figure 7 and tabulate in Table 5. We notice that during the first three epochs, that is, between days 64 and 127, the spectral indices are  $\alpha(1390/610) \sim 1.4$ . This value is much flatter than the spectral index 2.5 expected in the SSA model or the steeper value in the FFA model. The values of  $\alpha(610/325) \geq 1.16$  are a lower limit on day  $\sim 289$ , which is also consistent with the above values.

While the spectral indices are expected to flatten near the spectral peaks, the 1390 MHz peak occurs at day 126 and the 610 MHz peak much later (see Section 4.1). Thus only the last data point around 127 days may be affected by this effect. The fact that the spectral indices have flatter values from 64 days

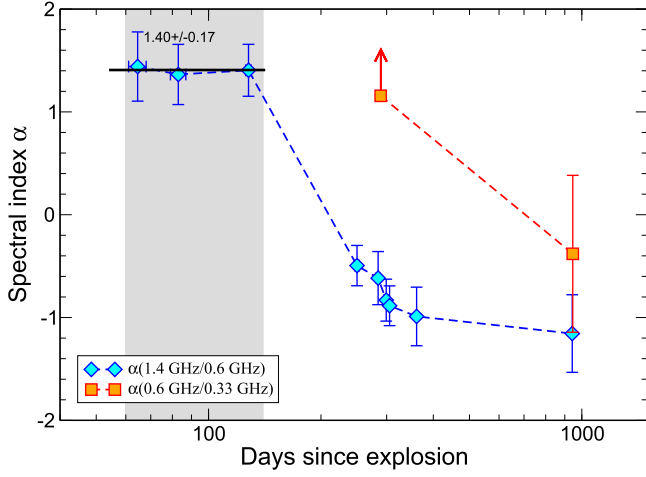


**Figure 7.** Spectral index evolution between 1390 and 610 MHz (blue diamonds) and between 610 and 325 MHz bands (orange squares).

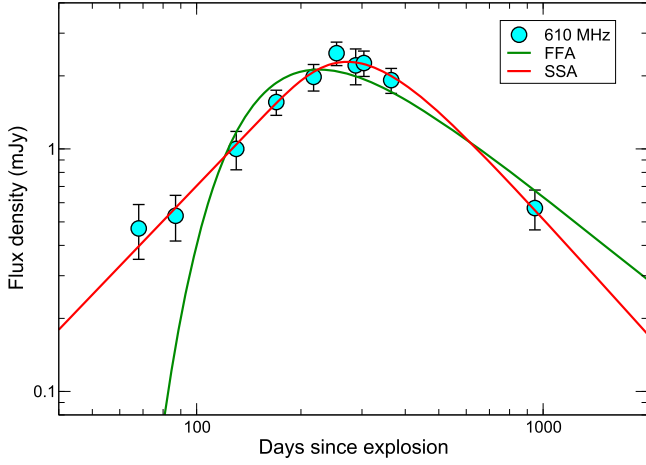


**Figure 8.** SSA model fit to the GMRT 610 MHz light curve. The data are dominated by the points in the optically thick part of the light curve.

onward indicates that this is a real effect. The average value of the optically thick spectral index from the first three epochs is  $1.40 \pm 0.17$  (Figure 7).

To probe the nature of absorption further, we look at the radio light curve at 610 MHz, the best sampled frequency in the optically thick phase. We again fit the standard FFA and SSA models, using Equations (5) and (6), respectively:

$$F(t)_{\text{FFA}} = K_1 \left( \frac{t}{100 \text{ days}} \right)^{-\beta} \left[ \exp \left( -K_2 \left( \frac{t}{100 \text{ days}} \right)^{-\delta} \right) \right] \quad (5)$$

$$F(t)_{\text{SSA}} = K_1 \left( \frac{t}{100 \text{ days}} \right)^{\beta'} \left[ 1 - \exp \left( -K_2 \left( \frac{t}{100 \text{ days}} \right)^{-(\beta'+\beta)} \right) \right]. \quad (6)$$

While the FFA model gives a poor fit, the SSA model seems to fit the data reasonably well (Figure 8). However, the best-fit values of  $\beta' = 1.49 \pm 0.12$  and  $\beta = 1.59 \pm 0.12$  obtained in these fits (column 3 of Table 4) will imply  $m = 0.55 \pm 0.06$  and  $p = 1.45 \pm 0.43$ . The value of  $p$  is unrealistically small and is inconsistent with the observations (Figure 4). The

**Table 5**  
Spectral Indices for Near-simultaneous Measurements at the GMRT Frequencies

Age <sup>a</sup> (days)	Spectral Index $\alpha_{1390/610 \text{ MHz}}$	Spectral Index $\alpha_{610/325 \text{ MHz}}$
$64.57 \pm 3.48$	$1.44 \pm 0.34$	...
$82.98 \pm 3.94$	$1.36 \pm 0.29$	...
$127.92 \pm 2.17$	$1.40 \pm 0.25$	...
$249.92 \pm 3.50$	$-0.49 \pm 0.20$	...
$284.58 \pm 3.15$	$-0.62 \pm 0.26$	...
$289.12 \pm 1.39$	...	$\geq 1.16$
$299.18 \pm 4.64$	$-0.83 \pm 0.20$	...
$305.46 \pm 1.64$	$-0.89 \pm 0.20^b$	...
$360.89 \pm 3.44$	$-0.99 \pm 0.29$	...
$942.55 \pm 4.00$	$-1.16 \pm 0.37$	...
$945.54 \pm 1.01$	...	$-0.76 \pm 0.69$

**Notes.**

<sup>a</sup> The age is calculated assuming 2014 September 26 (UT) as the date of explosion. The range in the epochs reflects the time span of the near-simultaneous measurements.

<sup>b</sup> With VLA 1.5 GHz measurement.

derived value of  $m$  is much smaller than the typical values seen in SNe Ib and will indicate very high deceleration at this young age, which is unlikely. Hence we conclude that despite providing acceptable fit, the standard SSA model does not represent a physically viable model for the 610 MHz light curve.

Unphysical values of model parameters obtained above combined with the much flatter spectral index in the optically thin phase,  $\alpha' = 1.4 \pm 0.17$ , indicate that the standard homogeneous SSA emission model does not fit the radio emission in SN J1204.

### 5.1. An Inhomogeneous Model

Björnsson (2013) and Björnsson & Keshavarzi (2017) have explained the flatter optically thick evolution of the radio spectra in terms of inhomogeneities in the radio-emitting region caused by the variations in the distribution of magnetic fields and relativistic electrons. Björnsson & Keshavarzi (2017) have shown that if the emission structure is inhomogeneous, then fitting a standard homogeneous model to observations around the peak frequency gives a lower limit to the source radius. Björnsson (2013) and Björnsson & Keshavarzi (2017) have quantified the variation of the magnetic field over the projected source surface by a source covering factor,  $f_{B,\text{cov}}$ . As per their formulation, even though the locally emitted spectrum is that of a standard synchrotron, the  $f_{B,\text{cov}}$  will give rise to a range of optical depths over the source, broadening the observed spectrum. Since the covering factor is maximum at frequencies substantially below that of the spectral peak (Björnsson & Keshavarzi 2017), the detailed observations at low frequencies are best to probe the inhomogeneities.

In Appendix A, we develop an inhomogeneous emission model adopted from Björnsson & Keshavarzi (2017). As per this formulation, the inhomogeneous model will alter the spectra for magnetic fields ranging  $B_0 < B < B_1$  (Figure 14), and radio emission will follow the standard homogeneous SSA formulation at frequencies corresponding to magnetic fields

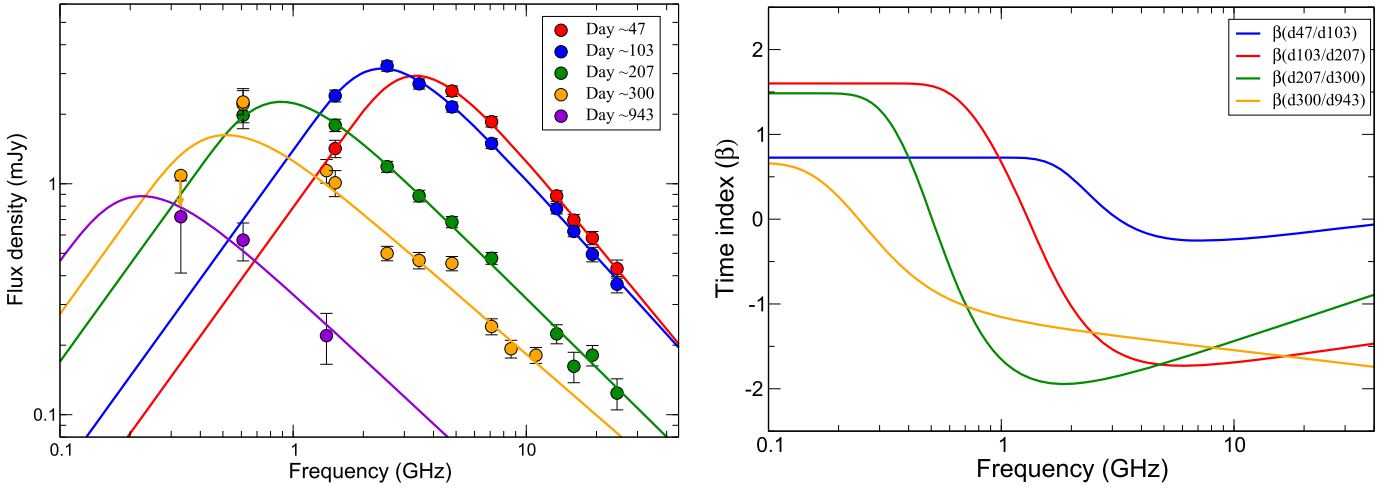


**Figure 9.** Left panel: inhomogeneous SSA model fit to individual spectra of SN J1204 on days 47, 103, 207, 300, and 943, respectively. In the right panel, we plot the evolution of temporal index  $\beta$  as a function of frequency.

outside this range, that is,

$$F(\nu) \propto \begin{cases} \nu^{\frac{5}{2}}, & \nu < \nu_{\text{abs}}(B_0) \\ \nu^{\frac{3p+7+5\delta'-a(p+4)}{p+2(1+\delta')}}, & \nu_{\text{abs}}(B_0) < \nu < \nu_{\text{abs}}(B_1) \\ \nu^{-\frac{(p-1)}{2}}, & \nu > \nu_{\text{abs}}(B_1). \end{cases} \quad (7)$$

Here  $\nu_{\text{abs}}$  is the SSA frequency,  $a$  is defined as  $P(B) \propto B^{-a}$ , where  $P(B)$  is the probability of finding a particular value of  $B$  within  $B$  and  $B + dB$  (Equation (13)). We define  $\alpha'$  as the spectral index in the SSA optically thick phase in the inhomogeneous model. Thus in our case  $\alpha' \equiv (3p + 7 + 5\delta' - a(p + 4)) / (p + 2(1 + \delta')) = 1.4$ . Here  $\delta'$  indicates a correlation between the distribution of relativistic electrons with the distribution of magnetic field strengths (see Appendix A). For  $\delta' = 0$  the inhomogeneities in the relativistic electrons distribution are not correlated with the inhomogeneities in the magnetic field. For  $\delta' = 1$ , the inhomogeneities between the two distributions are correlated.

Since our radio observations in the optically thick phase indicate  $\alpha' < 5/2$  at all epochs, this suggests we are in the regime  $\nu > \nu_{\text{abs}}(B_0)$  for observed frequency range. For the observed  $F_\nu \sim \nu^{1.4}$  in the optically thick phase, and for  $p = 3$ , we obtain  $a = 1.3$  for  $\delta' = 0$  and  $a = 1.6$  for  $\delta' = 1$ .

In order to take the inhomogeneities into account, we use a model in which the optically thick spectral index follows  $\alpha' = 1.4$  in Equations (3) and (4):

$$F(\nu, t) = K_1 \left( \frac{\nu}{1 \text{ GHz}} \right)^{\alpha'} \left( \frac{t}{100 \text{ day}} \right)^{\beta'} (1 - e^{-\tau_{\text{ssa}}(\nu, t)}), \quad (8)$$

where the optical depth is characterized by the SSA due to the relativistic electrons at the forward shock. The SSA optical depth  $\tau_{\text{ssa}}$  is given by

$$\tau_{\text{ssa}}(\nu, t) = K_2 \left( \frac{\nu}{1 \text{ GHz}} \right)^{-(\alpha' + \frac{p-1}{2})} \left( \frac{t}{100 \text{ day}} \right)^{-(\beta' + \beta)}. \quad (9)$$

The best-fit values are tabulated in column 4 of Table 4. We plot the best-fit inhomogeneous model in Figures 5 and 6. While the inhomogeneous model fits are better than the standard SSA and FFA fits, and  $\chi^2_\nu$  improved by nearly a factor

of  $\sim 2$ , the early data still deviate from the inhomogeneous SSA model. Figure 6 indicates that the model spectrum on day  $\sim 47$  does not represent the data well. The model light curves at early epochs are also discrepant with the data (Figure 5).

This suggests that a global model assuming constant  $\beta'$ ,  $\beta$ , and  $p$  will not fit the data well at all the epochs. This situation can be reconciled if there is an evolution in the blast-wave parameters with time, likely at early epochs.

### 5.2. Shock Passing through a Shell

To understand the dynamical evolution of the blast wave and to investigate the inconsistency with the global fit parameters, we study the near-simultaneous spectra of the SN at individual epochs (Figure 9). Since we established the need for an inhomogeneous model in Section 5.1, we model the spectra of SN J1204 at each epoch with the inhomogeneous SSA model:

$$F(\nu) = 1.582 F_{\text{abs}} \left( \frac{\nu}{\nu_{\text{abs}}} \right)^{\alpha'} \left[ 1 - \exp \left( - \left( \frac{\nu}{\nu_{\text{abs}}} \right)^{-(\alpha' + \alpha)} \right) \right], \quad (10)$$

where we use  $\alpha' \equiv 1.4$ .  $F_{\text{abs}}$  is the peak flux density at a frequency  $\nu_{\text{abs}}$  at a given epoch.

There are a few things to decipher from the individual spectra. The spectra evolve very little between days  $\sim 47$  and  $\sim 103$  (Figure 9). The peak flux density  $F_{\text{abs}}$  and peak frequency  $\nu_{\text{abs}}$  have a nearly flat evolution  $F_{\text{abs}} \propto t^{0.24 \pm 0.08}$  and  $\nu_{\text{abs}} \propto t^{-0.38 \pm 0.06}$  between these two epochs. In addition, we note that there are seven and eight independent data points in spectra on day 47 and 103, respectively, and all of these data are consistent with much slower evolution than expected in the standard synchrotron emission model. This can also be seen in the time evolution plot, where  $\beta$  is close to zero at high frequencies during these two epochs. Such a situation may arise if the shock is crossing through a shell and has slowed down due to a high density of the shell, causing the time evolution of the parameters to slow down between these two epochs.

While it is difficult to decipher the exact duration for which the shock is passing through the shell, we attempt to constrain it based on our radio data. For this purpose, we replot the light curve zooming into early times (Figure 10). Figure 10 indicates that while the flux density in the earliest data between days 35

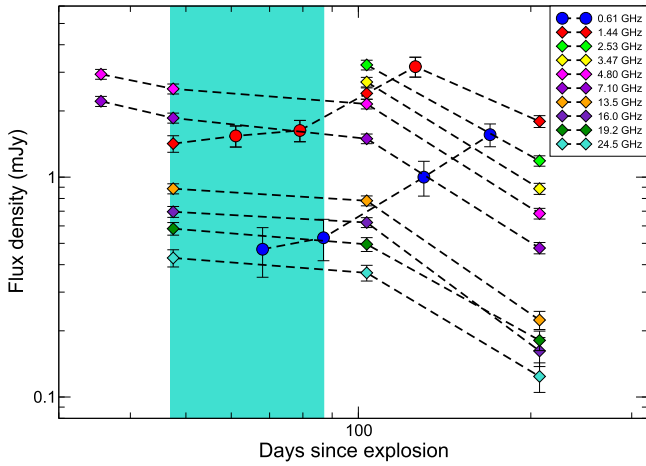


**Figure 10.** Radio light curves of SN J1204 up to day  $\sim 200$ .

and 47 evolves as  $t_{(4.8 \text{ GHz})}^{-0.53 \pm 0.25}$  and  $t_{(7.1 \text{ GHz})}^{-0.60 \pm 0.25}$  at 4.8 and 7.1 GHz bands, respectively, the evolution of the flux density slows down as  $t_{(4.8 \text{ GHz})}^{-0.20 \pm 0.09}$  and  $t_{(7.1 \text{ GHz})}^{-0.28 \pm 0.09}$  between days 47 and 103, respectively. This again steepens and evolves as  $t_{(4.8 \text{ GHz})}^{-1.65 \pm 0.12}$  and  $t_{(7.1 \text{ GHz})}^{-1.65 \pm 0.12}$  after day 110. While the relatively flatter evolution between 35 and 47 days at the 4.8 and 7.1 GHz bands could be reconciled with a situation where we may be witnessing the shock soon after the peak transition at these frequencies and tracing the broader top likely due to inhomogeneities, the significant flattening between days 47 and 103 cannot be explained in this framework.

This suggests that shock was probably moving into a smooth CSM at the first epoch  $d \sim 35$  but entered into a higher density shell some time during  $d \sim 47$ . The steep evolution between days 103 and 207 suggests that it was out of the shell by the time VLA observations commenced on  $d \sim 103$ . An additional clue on the length of time it took for the shock to cross the shell comes from the optically thick data points at the 1.4 and 0.6 GHz bands. The first three epochs at 1.4 GHz light curves (covering  $\sim 79$  days) and first two epochs at 0.61 GHz (covering  $\sim 87$  days) are flatter than the other optically thick data points at this frequency (Figure 10). This indicates that the shock likely stayed in the dense shell up to  $t \sim 87$  days and was out of the shell afterward. Thus we infer that the shock likely remained in the shell for 47–87 days after the SN explosion. However, we note that the transition at day  $\sim 47$  is much less secure than that at day  $\sim 87$ .

After emerging from the shell, the shock velocity is expected to stay roughly constant (van Marle et al. 2010) or even accelerate (Harris et al. 2016). This transition phase may last a few dynamical timescales, that is, until the swept-up mass starts to dominate the extra mass in the shell. Regardless of the details of this phase, the time evolution of  $\nu_{\text{abs}}$  should speed up and approach that pertaining to the time before the shock entered the shell.

In order to evaluate the possible effects of FFA after the shock entered the shell, we examine  $\tau_{\text{ffa}}(\nu_{\text{abs}})$ , which is the FFA optical depth at  $\nu_{\text{abs}}$ . As discussed by Björnsson & Lundqvist (2014), this is a maximum value for the free-free optical depth  $\tau_{\text{ffa}}$ , because it is set by the temperature resulting from the actual heating due to the absorbed synchrotron emission itself.

Neglecting terms of order unity,  $\tau_{\text{ffa}}(\nu_{\text{abs}})$  is (Björnsson & Lundqvist 2014)

$$\tau_{\text{ffa}}(\nu_{\text{abs}}) \sim 3 \left( \frac{v_{\text{sh}}}{10^4 \text{ km s}^{-1}} \right)^{-9/5} \left( \frac{t}{10 \text{ days}} \right)^{-12/5} \times \left( \frac{\nu_{\text{abs}}}{10 \text{ GHz}} \right)^{-13/5} \left( \frac{\dot{M}_{-5}}{v_{w,1}} \right)^{7/5}, \quad (11)$$

where  $v_{\text{sh}}$  is the velocity of the forward shock in kilometers per second. The density of the CSM is  $\propto \dot{M}_{-5}/v_{w,1}$ , where  $\dot{M}_{-5}$  is the steady mass-loss rate of the progenitor star in units of  $10^{-5}$  solar masses per year and  $v_{w,1}$  is the corresponding wind velocity in units of  $10 \text{ km s}^{-1}$ , respectively. Since it is likely that the shock velocity is larger than  $10^4 \text{ km s}^{-1}$  at  $t \sim 47$  days and  $\nu_{\text{abs}} = 3.5 \text{ GHz}$  on this day (Figure 9), Equation (11) implies

$$\tau_{\text{ffa}}(\nu_{\text{abs}}) < 1 \times \left( \frac{\dot{M}_{-5}}{v_{w,1}} \right)^{7/5}. \quad (12)$$

Since SN J1204 is an SN Ib,  $v_{w,1} \gg 1$  is expected. Unless the mass-loss rate is unusually large (i.e.,  $\dot{M}_{-5} \gg 1$ ), FFA should be negligible in the wind; for example, a wind velocity of  $10^3 \text{ km s}^{-1}$  and  $\dot{M}_{-5} = 1$  give  $\tau_{\text{ffa}}(\nu_{\text{abs}}) = 1.6 \times 10^{-3}$ .

Although hydrodynamical simulations are needed to describe the passage of the shock through the shell, Equation (11) can be used to estimate its FFA. Initially, when the forward shock impacts the shell, the already shocked mass between the forward and reverse shocks will act as a piston. The shock velocity in the shell is then given, roughly, by momentum conservation, that is, the shock velocity slows down by a factor  $(\rho/\rho_0)^{1/2}$ . Here,  $\rho$  is the shell density and  $\rho_0$  is the density behind the forward shock at impact. Furthermore, observations show that the duration of the shell passage is roughly equal to the time for the forward shock to reach the shell. The width of the shell is then  $\Delta R \approx R (\rho_0/\rho)^{1/2}$ . The FFA of the shell can then be obtained by multiplying the right-hand side of Equation (11) with  $(\rho/\rho_0)^{7/5}$  ( $\Delta R/R = (\rho/\rho_0)^{9/10}$ ; for example, with  $v_{w,1} = 10^2$  and  $\dot{M}_{-5} = 1$ , an FFA optical depth of unity in the shell corresponds to  $\rho/\rho_0 \approx 1.3 \times 10^3$ . For a strong shock, the density in the wind is  $\rho_0/4$ , which gives a density contrast between the shell and the wind of  $3.2 \times 10^2$ . Furthermore, the associated slowdown of the shock velocity would be by a factor 38. In the standard model, the values of  $\nu_{\text{abs}}$  and  $F(\nu)$  are expected to evolve roughly inversely with time (see also the analytical fits above). As shown in Figures 9 and 10, the observed slowdown is substantially less than this. Hence, the optical depth to FFA in the shell should also be substantially below unity at 3.5 GHz, and the density contrast between the shell and the wind is expected to be less than  $10^2$ .

There is another puzzle. If the shock is passing through a dense shell, one would expect the optically thin emission to increase due to the continuous injection of relativistic electrons. But Figure 10 clearly shows that the flux evolution at 4.8 GHz and higher frequencies is flatter and optically thin. This could have been explained by cooling, but Figure 4B indicates that the optically thin spectral indices are mostly consistent with near constant values and do not show any particular steepening in this duration. Thus cooling is unlikely to be the reason for flatter optically thin light curves. Björnsson (2013) has explained this situation where a constant magnetic field is

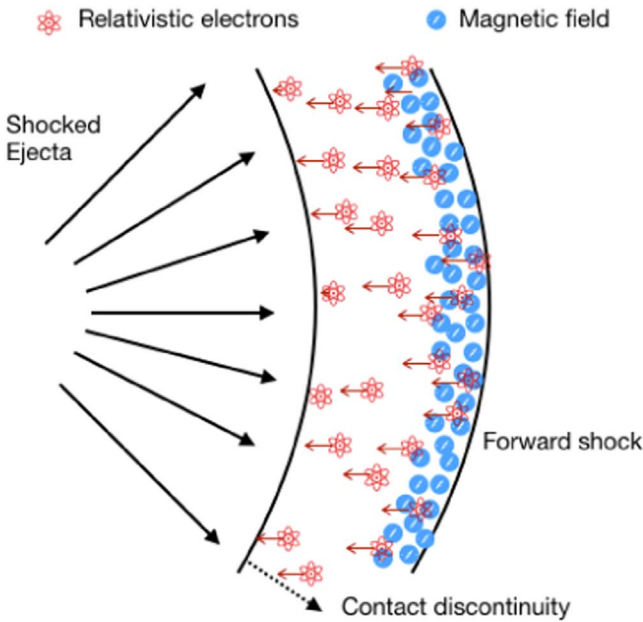


**Figure 11.** Cartoon diagram of a situation where relativistic electrons are homogeneously distributed but magnetic field is not. The near constant magnetic field is confined within a small distance from the shock front. Here one can obtain a case where the main contributions to both emission and self-absorption come from near the shock boundary and give rise to flat light curves seen at the VLA frequencies.

confined within a small distance from the shock front in the inhomogeneous model (their Equation (4)). In such a case, relativistic electrons are continuously entering the shocked shell and cascading downward, hence leaving the width of the radio-emitting region almost constant. Thus the main contributions to both emission and absorption come from near the shock boundary and give rise to the flat light curves seen at the VLA frequencies. This would then be consistent with a situation where the inhomogeneities are confined mainly to the magnetic field distribution, whereas the relativistic electrons are distributed more or less uniformly (Figure 11). If this is indeed the case, it suggests  $\delta' \approx 0$  in Equation (7).

### 5.3. Combining with the Multiwavelength Data

The *Swift*-XRT data covered the epochs between days 33 and 1128 since explosion; however, the most important constraints come from the *Chandra* data on day 51. At such early times, inverse Compton scattering of photospheric photons can contribute significantly to the X-ray emission in SNe Ib/c, and this prediction can be tested.

In Figure 12, we plot the radio, X-ray, and optical luminosities for SN J1204. The X-ray luminosity is at least 3 orders of magnitude lower than the optical luminosity. Björnsson (2013) estimated a quantity  $(L_x/L_{\text{bol}})^2/L_r$ , where  $L_x$ ,  $L_{\text{bol}}$ , and  $L_r$  are the X-ray, bolometric, and radio luminosities, respectively, normalized to their respective values for another stripped-envelope SN 2003L. They found that this quantity does not change significantly for various SNe Ib/c and remains close to 1, even though the individual values of  $L_x$ ,  $L_{\text{bol}}$ , and  $L_r$  are very different. With the lack of X-ray detection as well as unavailability of measurement of bolometric luminosity in SN J1204, we cannot measure this parameter. However, the observations with *Chandra* around day 51 give the most constraining upper limits on the X-ray luminosity, and the ASAS-SN data in the V-band

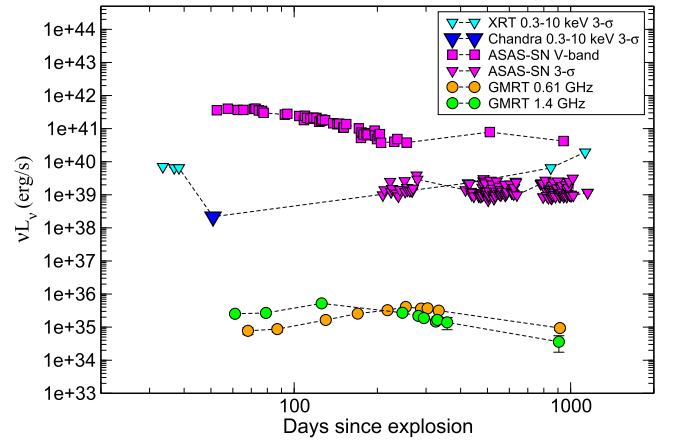


**Figure 12.** A plot for  $\nu L_\nu$  luminosities at various wavelengths against time. The SN is not detected in the X-ray bands. *Chandra* observations around day 51 (the bigger blue triangle) provide the most stringent upper limits on the X-ray luminosity.

can be treated as a lower limit on  $L_{\text{bol}}$ . Using these values, we can constrain the above ratio,  $(L_x/L_{\text{bol}})^2/L_r$  for SN J1204, scaled to the respective values for SN 2003L (Soderberg et al. 2006), to be  $(L_x/L_{\text{bol}})^2/L_r < 11.51$ . This is indeed an upper limit, and the actual value could be much smaller and may fit in with the values obtained from other SNe Ib/c (Figure 1 of Björnsson 2013). Björnsson (2013) also found this quantity  $(L_x/L_{\text{bol}})^2/L_r$  to not evolve with time significantly, suggesting that  $L_r \propto (L_x/L_{\text{bol}})^2$ . This is consistent with a scenario in which a substantial contribution to the X-rays come from inverse Compton scattering of photospheric photons (Björnsson 2013). Thus an inverse Compton scenario implies an inhomogeneous source structure or vice versa, if the equipartition fraction is not too far away from unity (Equation (22) of Björnsson 2013).

### 5.4. Final Comprehensive Model

Connecting all the pieces together as discussed in the previous sections, we establish that the radio emission from SN J1204 is arising from the shock, which has inhomogeneities, and is passing through a shell during days 47–87 since explosion. Hence we fit the inhomogeneous SSA model excluding all the data until day 87. We again use the formalism described in Equations (8) and (9). The best-fit model parameters are detailed in column 5 of Table 4. While the  $\chi^2 = 1.6$  is still not a statistically very good fit, we consider it a reasonably acceptable fit. We plot the spectra at four representative days, and the light curve at four representative frequencies in Figure 13. Here the shaded region in the light curves indicates the data excluded from the modeling. These figures indicate that the inhomogeneous model fits the data reasonably well. Unfortunately, it is difficult to quantitatively constrain the data before day 87.

## 6. Discussion and Conclusions

In this paper we have described the radio observations of SN J1204 up to around 1200 days after the explosion, covering the frequency range from 0.33 to 25 GHz. The radio observations of SN J1204 suggest that the radio-emitting region is inhomogeneous where the magnetic field is confined within a small distance from the shock front. The data reveal that the shock is passing through a shell during  $\sim 47$  to  $\sim 87$  days.

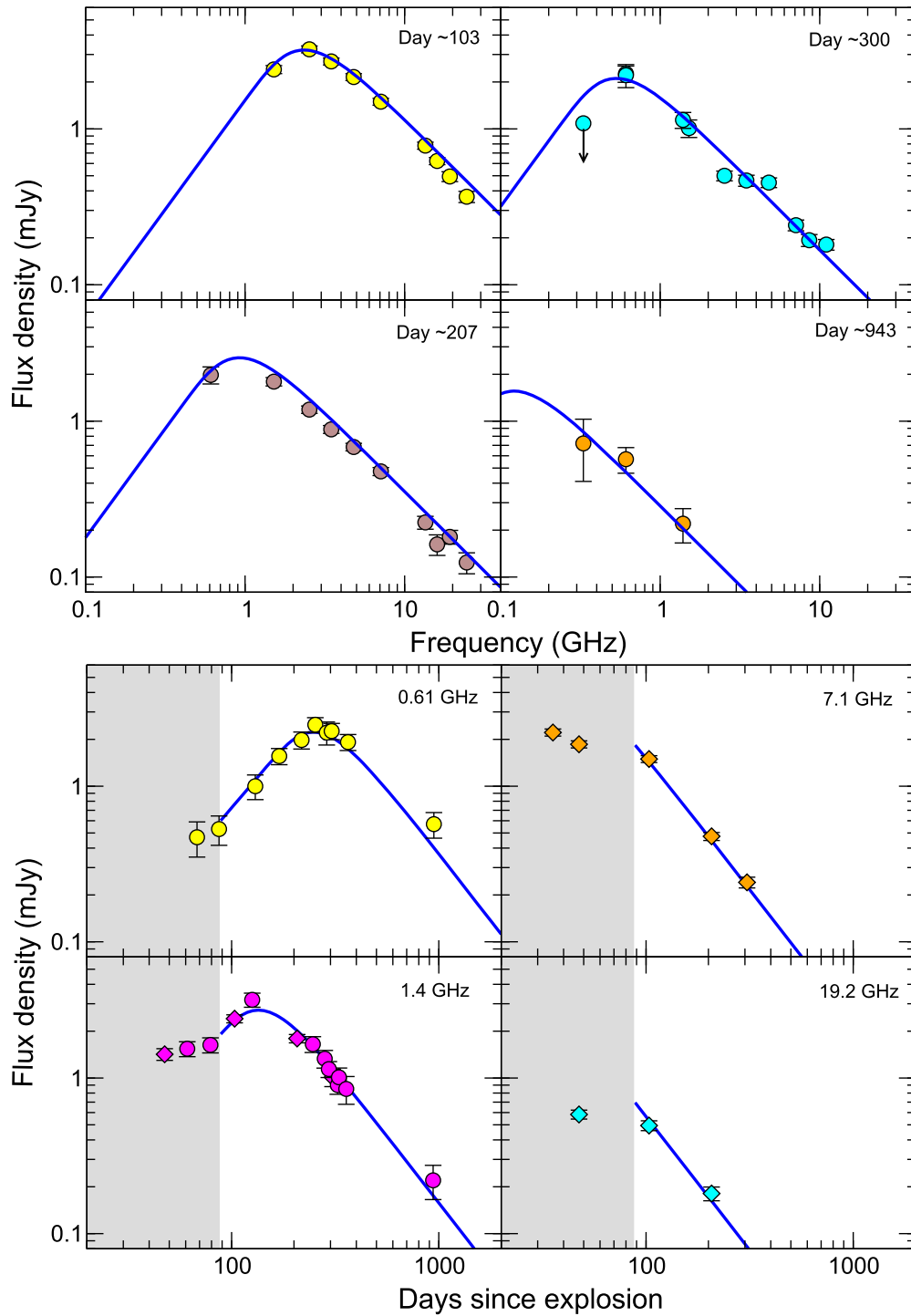


**Figure 13.** The best-fit inhomogeneous SSA model excluding data before 87 days. Here the shaded region in the light curves indicated the data excluded from the modeling. The best-fit spectra (upper panel) and best-fit light curves (lower panel) are plotted at four representative days and frequencies, respectively.

The GMRT low-frequency data in the optically thick phase are crucial to indicate the presence of inhomogeneities in the synchrotron-emitting region, which is responsible for the flattening of the optically thick spectral index to  $\sim 1.4$ . Flattened light curves and spectra have been seen in several SNe Ib/c, for example, SNe 1994I (Weiler et al. 2011), 2003L (Soderberg et al. 2005), and so on. Weiler et al. (2011) explained the flattened profile in SN 1994I due to an FFA process intrinsic to the synchrotron-emitting source with the thermal electrons distributed roughly as the relativistic ones;

however, this scenario within the standard synchrotron model gives discrepant results (Björnsson & Keshavarzi 2017). While such an intrinsic FFA mechanism is possible in SNe II<sub>n</sub> due to their high densities (e.g., Chandra et al. 2012), it is very unlikely in SNe Ib/c, which are expected to have W-R progenitors.

The ratio of  $(L_x/L_{\text{bol}})^2/L_r$  for SN J1204, where  $L_x$ ,  $L_{\text{bol}}$ , and  $L_r$  are normalized to their respective values for SN 2003L, is  $< 11$ . However, it is an overestimation because we use the X-ray upper limit to substitute for the X-ray luminosity and

ASAS-SN *V*-band luminosity as a proxy for bolometric luminosity. Hence our value of  $(L_x/L_{\text{bol}})^2/L_r < 11$  is not discrepant with other SNe Ib/c, indicating inverse Compton effects likely to be important when the shock has inhomogeneities (Björnsson 2013).

Since our radio observations cover a large span of time, we have been able to fit the individual spectra up to around  $\sim 1200$  days postexplosion. The spectra between days 47 and 103 suggest rather insignificant time evolution in the shock parameters (Figure 9). We have explained this in a scenario in which the shock is moving through a higher density shell between  $\sim 47$  and  $\sim 87$  days. We show in Section 5.2 that the FFA optical depth in the shell is not expected to increase by more than a factor of 2 and is likely to not alter the radio spectra significantly. Recently published optical spectroscopic data by Singh et al. (2019) indicate no obvious new features associated with the shock impacting the shell. This indicates that the emission comes mainly from the ejecta and that the contribution from the shocked material is negligible. The lack of any signs of the shell interaction would then be consistent with a rather low shell mass, that is, a low FFA optical depth.

A major issue here is that when the shock is crossing the shell, one would assume the optically thin flux to increase in this duration due to continuous injection of electrons. This is contrary to what VLA data reveal, that is, flatter optically thin light curves. While this situation could have been reconciled in the presence of cooling, our data have suggested an absence of cooling. We find that the early time flatter optically thin light-curve evolution during the shell-crossing phase is consistent with a scenario where the magnetic field distribution is confined within a small region of the shock, whereas the relativistic electrons are distributed more uniformly and the width of emission region stays nearly constant (Figure 11).

SNe Ib/c are understood to be explosions of massive stars whose hydrogen envelopes have been stripped off before the explosion (Woosley et al. 2002), but the physics of the process by which stars lose their outer envelopes and the corresponding timescales are still debated (Smith et al. 2011). The presence of a shell during  $\sim 47$  to  $\sim 87$  days in SN J1204 could be a clue to the stripping of the hydrogen/helium shell of the progenitor, possibly from a binary system (Podsiadlowski et al. 1992). Evidence of this has been seen for SNe Ib/c SN 2001em (Soderberg et al. 2004) and SN 2014C (Vinko et al. 2017), where evidence of Balmer recombination lines has been seen. In SNe 2001em and 2014C, the flux density enhancement was observed at a late time, that is,  $\sim$ day 677 for SN 2001em (Stockdale et al. 2005; Chugai & Chevalier 2006) and  $\sim$ day 400 for SN 2014C (Anderson et al. 2017). This suggested that the shells were ejected several decades before the explosion. However, in case of SN J1204, we find the evidence of dense shell just 47 days after the explosion, lasting for  $\leq 40$  days. Due to lack of constraints on ejecta and wind velocity, we cannot determine the preexplosion epoch at which the shell was ejected, but it could not have been too long ago, unlike SNe 2001em and 2014C, as W-R are known to have fast winds. We have checked the archival ASAS-SN data to search for possible signatures of pre-SN ejection. The ASAS-SN *V*-magnitude photometric observations begin  $\sim 600$  days pre-SN and do not show evidence of pre-SN ejection episodes (Figure 2); however, there are no data at many epochs. Recent campaigns to observe SNe within days of explosion have revealed narrow emission

lines of high-ionization species in the earliest spectra of luminous SNe II of all subclasses. These flash ionization features indicate the presence of a high-density medium close to the progenitor star (Hosseinzadeh et al. 2018). In our case, the SN was detected after the optical maximum, and hence no such data are available.

The optically thin spectral index remains close to  $-1$  at all epochs. This would suggest  $p \approx 3$ , which is steeper than expected ( $p \approx 2$ ) from the standard diffusive shock acceleration theory. In the absence of cooling, this situation can be reconciled if the diffusive shock acceleration is so efficient that the whole process becomes nonlinear (Chevalier & Fransson 2006, 2017). The prediction of such a process is a flatter  $p$  profile with time, albeit evolving very slowly (Chevalier & Fransson 2006, 2017). This can be tested at late-epoch low-frequency observations.

In Appendix C, we have derived the evolution of covering factor  $f_{\text{B,cov}}$ . For SN J1204,  $\beta' - \alpha'$  is positive, indicating that the time evolution for  $f_{\text{B,cov}}$  is positive (Equation (28)). This means the inhomogeneities should smooth out if followed long enough. We are continuing to observe SN J1204 at GMRT frequencies, especially at the 325 MHz band, and these observations will test the above hypothesis and reveal whether the synchrotron-emitting region has emerged into a homogeneous one at late epochs.

To summarize the main conclusions of this work, the radiofrequency observations of SN J1204 have revealed that the radio emission is arising from a shock, with inhomogeneities mainly in the magnetic field distribution behind the shock (as sketched in Figure 11). This shock is passing through a higher density shell during the time frame of  $\sim 47$  to  $\sim 87$  days. Low-frequency sensitive telescopes like GMRT provide excellent opportunity to carry out such low-frequency studies to reveal the nature of synchrotron-emitting regions. With 3 times increased sensitivity as well as the near-continuous and low-frequency wide bands of the upgraded GMRT (Gupta et al. 2017), such studies will be possible for a large number of SNe in the future.

We thank the referee for constructive comments, which helped improve the manuscript significantly. We acknowledge substantial help from Subo Dong, Jose L. Prieto, Krzysztof Z. Stanek, Christopher Kochanek, Todd Thompson, and Tom Holoiu for the ASAS-SN data as well as Roger A. Chevalier. P.C. acknowledges support from the Department of Science and Technology via a Swarana Jayanti Fellowship award (file no. DST/SJF/PSA-01/2014-15). A.R. acknowledges a Raja Ramana Fellowship of DAE, from the Government of India. We thank the staff of the GMRT that made these observations possible. GMRT is run by the National Centre for Radio Astrophysics of the Tata Institute of Fundamental Research. The National Radio Astronomy Observatory is a facility of the National Science Foundation operated under cooperative agreement by Associated Universities, Inc. This research has made use of data obtained through the High Energy Astrophysics Science Archive Research Center Online Service, provided by the NASA/Goddard Space Flight Center.

*Facilities:* Giant Metrewave Radio Telescope, Karl J. Jansky Very Large Array, Chandra X-ray Telescope, Swift X-ray Telescope.

## Appendix A Inhomogeneous Spherically Symmetric Model

In a homogeneous spherically symmetric model for SNe Ib/c, the radio emission is usually fit with a synchrotron emission model, suppressed at early times by SSA with a frequency dependence of the flux density of  $F_\nu \propto \nu^{2.5}$ . However, inhomogeneities in an otherwise spherically symmetric emission structure can cause broadening in the observed radio spectra and/or light curves (Björnsson 2013). SSA frequency is quite sensitive to the presence of inhomogeneities and can be used to identify these in the source structure.

The inhomogeneities can arise by variations in the relativistic electrons distribution and/or the magnetic field strength within the synchrotron source. Björnsson & Keshavarzi (2017) have derived the formalism for the inhomogeneous synchrotron source, assuming planar geometry, in terms of the covering factor  $f_{B,\text{cov}}$  characterizing the optically thick properties and the filling factor  $f_{B,\text{vol}}$  characterizing the optically thin properties of the radio emission. Here we discuss the relevant formalism taken mainly from Björnsson (2013) and Björnsson & Keshavarzi (2017) in the context of this paper. Here it is assumed that the locally emitted spectrum is that of the standard synchrotron model; however, the inhomogeneities in the magnetic field ( $B$ ) will give rise to variation in optical depths, and superposition of spectra with varying optical depths will broaden the resulting spectrum.

The source covering factor  $f_{B,\text{cov}}$  has been defined to describe the variation of the average magnetic field strength over the projected source surface. If  $P(B)$  is the probability of finding a particular value of  $B$  within  $B$  and  $B + dB$ , then the source covering factor will be parameterized from  $P(B) \propto B^{-a}$  and can be written as

$$f_{B,\text{cov}} \approx f_{B_0,\text{cov}} \left( \frac{B}{B_0} \right)^{1-a}. \quad (13)$$

Here we define magnetic field  $B_0$  such that frequencies smaller than the frequency corresponding to SSA at  $B_0$ , that is,  $\nu < \nu_{\text{abs}}(B_0)$ , follow the standard synchrotron model in the optically thick phase, and  $B_1$  such that frequencies larger than the frequency corresponding to SSA at  $B_1$ , that is,  $\nu > \nu_{\text{abs}}(B_1)$ , follow the standard synchrotron model in the optically thin phase (Figure 14). Between these two boundaries, the covering factor will modify the spectral flux as

$$F(\nu) \propto \frac{R^2 \nu^{5/2} f_{B,\text{cov}}}{B^{1/2}}. \quad (14)$$

The frequency dependence follows (Björnsson & Keshavarzi 2017):

$$\nu^3 \approx \nu_{\text{abs}}^3(B) \propto U_e U_B r \left( \frac{\gamma_{\text{min}}}{\gamma} \right)^{p-2}, \quad (15)$$

where  $U_e$  and  $U_B$  are energy densities of electrons and magnetic field, respectively, and  $\gamma_{\text{min}}$  is the minimum Lorentz factor such that  $N(\gamma)d\gamma \propto \gamma^{-p}d\gamma$  for  $\gamma \geq \gamma_{\text{min}}$ . It is also possible that the inhomogeneities in the relativistic electron

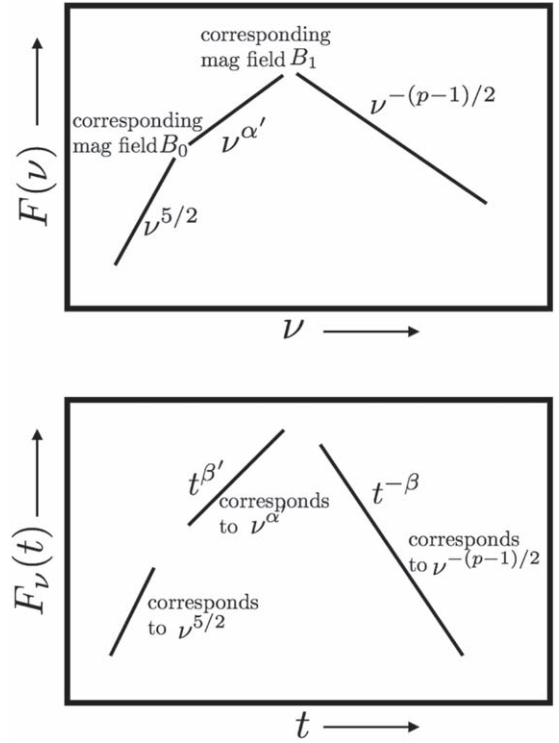


**Figure 14.** Cartoon diagram of an SN spectrum (above panel) for an inhomogeneous model. For  $\nu < \nu_{\text{abs}}(B_0)$ , the spectrum will follow the standard synchrotron model in the optically thick phase ( $F_\nu \propto \nu^{5/2}$ ). At the same time frequencies larger than the frequency corresponding to SSA at  $B_1$  (magnetic field at the peak), that is,  $\nu > \nu_{\text{abs}}(B_1)$ , follow the standard synchrotron model in the optically thin phase ( $F_\nu \propto \nu^{-(p-1)/2}$ ). Between these two boundaries, the spectrum will be affected by inhomogeneities and will follow  $F_\nu \propto \nu^{\alpha'}$  ( $\alpha' < 5/2$ ). The corresponding light curve (lower panel) will also get modified accordingly and show a flatter top.

distribution are correlated with the inhomogeneities in the magnetic field distribution. Björnsson & Keshavarzi (2017) define a parameter  $\delta'$ , which indicates a possible correlation between the inhomogeneous distribution of relativistic electrons with the distribution of magnetic field strengths,  $U_e r \gamma_{\text{min}}^{p-2} \propto B^{\delta'}$ . This gives

$$\nu_{\text{abs}}(B) = \nu_{\text{abs}}(B_0) \left( \frac{B}{B_0} \right)^{\frac{p+2(1+\delta')}{p+4}}. \quad (16)$$

Here  $\delta' = 0$  if no correlation exists between the two.

Combining the above, in the range  $\nu_{\text{abs}}(B_0) < \nu < \nu_{\text{abs}}(B_1)$ , the spectral flux density can be written as

$$\begin{aligned} F(\nu) &\approx F(\nu_{\text{abs}}(B_0)) \left( \frac{\nu}{\nu_{\text{abs}}(B_0)} \right)^{\frac{3p+7+5\delta'-a(p+4)}{p+2(1+\delta')}} \\ &\equiv F(\nu_{\text{abs}}(B_0)) \left( \frac{\nu}{\nu_{\text{abs}}(B_0)} \right)^{\alpha'}. \end{aligned} \quad (17)$$

Thus in case of inhomogeneous emission structure, the spectral flux density can be defined as

$$F(\nu) \propto \begin{cases} \nu^{\frac{5}{2}}, & \nu < \nu_{\text{abs}}(B_0) \\ \nu^{\alpha'} \text{ where } \alpha' \\ = \frac{3p + 7 + 5\delta' - a(p + 4)}{p + 2(1 + \delta')}, & \nu_{\text{abs}}(B_0) < \nu < \nu_{\text{abs}}(B_1) \\ \nu^{\frac{-(p-1)}{2}}, & \nu > \nu_{\text{abs}}(B_1). \end{cases} \quad (18)$$

The condition of  $\alpha' \leq 5/2$  and  $\alpha \geq -(p-1)/2$  indicates  $1/2 < a < (p+3)/2 + \delta'$ . Outside this range, the spectra are those of a homogeneous source.

For the inhomogeneous model, the size of the radio-emitting region  $R$  cannot be determined simply from the observed peak and frequency  $F(\nu_{\text{abs}}(B_0))$ ,  $\nu_{\text{abs}}(B_0)$ . One needs to substitute the homogeneous model equivalent peak flux  $F_{\text{homo}}(\nu_{\text{abs}}(B_0))$  with

$$F_{\text{homo}}(\nu_{\text{abs}}(B_0)) = F(\nu_{\text{abs}}(B_0))/f_{B_0,\text{cov}}, \quad (19)$$

which gives

$$R_p = 8.8 \times 10^{15} \left( \frac{U_e}{U_B} \right)^{-\frac{1}{19}} \left( \frac{F(\nu_{\text{abs}}(B_0))}{\text{Jy}} \right)^{\frac{9}{19}} \left( \frac{f_{B_0,\text{cov}}}{1} \right)^{-\frac{9}{19}} \\ \times \left( \frac{D}{\text{Mpc}} \right)^{\frac{18}{19}} \left( \frac{\nu_{\text{abs}}(B_0)}{5 \text{ GHz}} \right)^{-1} \text{ cm}. \quad (20)$$

The covering factor  $f_{B_0,\text{cov}}$  poses a large uncertainty; however, for spatially resolved inhomogeneous sources, the covering factor can be derived from the brightness temperature  $T_b$  ( $f_{B_0,\text{cov}}(\nu) \propto F(\nu)\nu^{-2}T_b^{-1}$ , Björnsson & Keshavarzi 2017), where  $T_b \propto \nu^{\frac{\delta-1}{p+2(1+\delta)}}$  in the transition region.

One can see that the inhomogeneous model comes at the cost of several extra parameters, that is,  $f_{B_0,\text{cov}}$ ,  $a$ ,  $B_1/B_0$ , and  $\delta'$ , which is hard to constrain despite well-sampled radio observations, especially for unresolved sources for which such extra parameters are degenerate toward the spectral width of the transition region.

## Appendix B

### Evolution of SSA Flux Density and Frequency

From the previous section (Appendix A), flux density in an inhomogeneous model is

$$F(\nu) = F(\nu_{\text{abs}}(B_1)) \left( \frac{\nu}{\nu_{\text{abs}}(B_1)} \right)^{\alpha'}. \quad (21)$$

One can determine the time evolution of the peak frequency and flux density from it. The above gives, for the optically thick part,

$$F(\nu, t) = F(\nu_{\text{abs}}(B_1), t) \times \nu_{\text{abs}}(B_1, t)^{-\alpha'} \propto t^{\beta'}. \quad (22)$$

And likewise for the optically thin part,

$$F(\nu, t) = F(\nu_{\text{abs}}(B_1), t) \times \nu_{\text{abs}}(B_1, t)^{(p-1)/2} \propto t^{-\beta}. \quad (23)$$

Combining Equations (16) and (17) gives

$$\nu_{\text{abs}}(B_1, t) \propto t^{-\frac{\beta'+\beta}{\alpha'+\frac{p-1}{2}}} \\ F(\nu_{\text{abs}}(B_1), t) \propto t^{\frac{\beta'-\alpha'-\frac{\beta'+\beta}{\alpha'+\frac{p-1}{2}}}{\alpha'+\frac{p-1}{2}}}. \quad (24)$$

Since the decline of  $\nu_{\text{abs}}(B_1, t)$  is very fast, it is clear that  $B_1$  should decline much faster than  $t^{-1}$  or  $R^{-1}$ . Hence  $B_1$  does not follow standard scalings, while  $B_0$  may still follow them.

## Appendix C

### Evolution of the Covering Factor

In order to determine the time evolution of  $f_{B_0,\text{cov}}$ , some assumptions are needed. Using Equation (22),

$$F(\nu_{\text{abs}}(B_0), t) \propto t^{\beta'} \nu_{\text{abs}}(B_0, t)^{\alpha'}. \quad (25)$$

For simplicity we assume  $U_e \propto U_B$  and  $F(\nu_{\text{abs}}(B_0), t) = f_{B_0,\text{cov}}(t) F_{\text{homo}}(\nu_{\text{abs}}(B_0), t)$  where  $F_{\text{homo}}(\nu_{\text{abs}}(B_0))$  is the flux density corresponding to a homogeneous emitting region. We can consider two cases: the magnetic and relativistic electron energy densities are proportional to the total postshock energy density, that is,  $B_0 \propto t^{-1}$ ; and another case of  $B_0 \propto R^{-1}$ , where the magnetic field corresponds to a case when the energy density is inversely proportional to its radiating surface:

1. Case (A):  $B_0 \propto t^{-1}$ , from Equation (5) of Chevalier (1998):  $\nu_{\text{abs}}(B_0, t) \propto B_0 \propto t^{-1-2\frac{(1-m)}{(p+4)}}$  and  $F_{\text{homo}}(\nu_{\text{abs}}(B_0), t) \propto t^{-(1-m)\frac{(2p+13)}{(p+4)}}$ . Hence using Equations (19) and (25),  $f_{B_0,\text{cov}}(t) \propto t^{\beta'} \nu_{\text{abs}}(B_0, t)^{\alpha'} F_{\text{homo}}(\nu_{\text{abs}}(B_0), t)^{-1}$  gives

$$f_{B_0,\text{cov}}(t) \propto t^{\beta'-\alpha'-2\alpha'\frac{(1-m)}{(p+4)}+(1-m)\frac{(2p+13)}{(p+4)}} \\ \propto t^{\beta'-\alpha'+(1-m)\frac{2(p-\alpha')+13}{p+4}}. \quad (26)$$

2. Case (B):  $B_0 \propto R^{-1}$  ( $R \propto t^m$ ), from Equation (6) of Chevalier (1998):  $\nu_{\text{abs}}(B_0, t) \propto t^{-m}$  and  $F_{\text{homo}}(\nu_{\text{abs}}(B_0), t) \propto t^0$ . Hence using Equations (19) and (25),

$$f_{B_0,\text{cov}}(t) \propto t^{\beta'} (t^{-m})^{\alpha'} \propto t^{\beta'-\alpha'm}. \quad (27)$$

Thus,

$$f_{B_0,\text{cov}}(t) \propto \begin{cases} t^{\beta'-\alpha'+(1-m)\frac{2(p-\alpha')+13}{p+4}}, & B_0 \propto t^{-1} \\ t^{\beta'-\alpha'+(1-m)\alpha'}, & B_0 \propto R^{-1} \propto t^{-m}. \end{cases} \quad (28)$$

If  $\beta' > \alpha'$ , the exponent is always positive; then one can see that  $f_{B_0,\text{cov}}(t)$  increases with time and hence inhomogeneities decrease with time irrespective of case A or B. Hence at late epochs, an inhomogeneous model is expected to make a transition into a homogeneous model for such cases.

## ORCID iDs

Poonam Chandra  <https://orcid.org/0000-0002-0844-6563>  
A. J. Nayana  <https://orcid.org/0000-0002-8070-5400>  
C.-I. Björnsson  <https://orcid.org/0000-0002-3284-4481>  
Francesco Taddia  <https://orcid.org/0000-0002-2387-6801>  
Peter Lundqvist  <https://orcid.org/0000-0002-3664-8082>

Alak K. Ray  <https://orcid.org/0000-0003-2404-0018>  
 Benjamin J. Shappee  <https://orcid.org/0000-0003-4631-1149>

## References

- Alard, C. 2000, *A&AS*, **144**, 363  
 Alard, C., & Lupton, R. H. 1998, *ApJ*, **503**, 325  
 Anderson, G. E., Horesh, A., Mooley, K. P., et al. 2017, *MNRAS*, **466**, 3648  
 Arnaud, K. A. 1996, *adass V*, **101**, 17  
 Björnsson, C.-I. 2013, *ApJ*, **769**, 65  
 Björnsson, C.-I., & Keshavarzi, S. T. 2017, *ApJ*, **841**, 12  
 Björnsson, C.-I., & Lundqvist, P. 2014, *ApJ*, **787**, 143  
 Cappa, C., Goss, W. M., & van der Hucht, K. A. 2004, *AJ*, **127**, 2885  
 Chandra, P., Chevalier, R. A., Chugai, N., et al. 2012, *ApJ*, **755**, 110  
 Chandra, P., & Kanekar, N. 2017, *ApJ*, **846**, 111  
 Chandra, P., Nayana, A. J., Ray, A., Yadav, N., & Chakraborti, S. 2014, *ATel*, **6755**, 1  
 Chevalier, R. A. 1982a, *ApJ*, **259**, 302  
 Chevalier, R. A. 1982b, *ApJ*, **258**, 790  
 Chevalier, R. A. 1996, in *ASP Conf. Ser. 93, Radio Emission from the Stars and the Sun*, ed. A. R. Taylor & J. M. A. Paredes (San Francisco, CA: ASP), **125**  
 Chevalier, R. A. 1998, *ApJ*, **499**, 810  
 Chevalier, R. A., & Fransson, C. 2006, *ApJ*, **651**, 381  
 Chevalier, R. A., & Fransson, C. 2017, in *Handbook of Supernovae*, ed. A. Alsabti & P. Murdin (Cham: Springer), **875**  
 Chugai, N. N., & Chevalier, R. A. 2006, *ApJ*, **641**, 1051  
 Clocchiatti, A., & Wheeler, J. C. 1997, *ApJ*, **491**, 375  
 Condon, J. J., Cotton, W. D., Greisen, E. W., et al. 1998, *AJ*, **115**, 1693  
 Dickey, & Lockman 1990, *ARA&A*, **28**, 215  
 Dopita, M. A., Cohen, M., Schwartz, R. D., & Evans, R. 1984, *ApJL*, **287**, L69  
 Ensmann, L. M., & Woosley, S. E. 1988, *ApJ*, **333**, 754  
 Evans, P. A., Beardmore, A. P., Page, K. L., et al. 2009, *MNRAS*, **397**, 1177  
 Fransson, C., & Björnsson, C.-I. 1998, *ApJ*, **509**, 861  
 Fruscione, A., McDowell, J., Allen, G. E., et al. 2006, *Proc. SPIE*, **6270**, 1  
 Goad, M. R., Tyler, L. G., Beardmore, A. P., et al. 2007, *A&A*, **476**, 1401  
 Gress, O., Denisenko, D., Lipunov, V., et al. 2014, *ATel*, **6634**, 1  
 Gupta, Y., Ajithkumar, B., Kale, H. S., et al. 2017, *CSci*, **113**, 707  
 Harris, C. E., Nugent, P. E., & Kasen, D. N. 2016, *ApJ*, **823**, 100  
 Helfand, D. J., White, R. L., & Becker, R. H. 2015, *ApJ*, **801**, 26  
 Henden, A. A., Levine, S., Terrell, D., & Welch, D. L. 2015, *AAS Meeting Abstracts*, **225**, 336.16  
 Hosseinzadeh, G., Valenti, S., McCully, C., et al. 2018, *ApJ*, **861**, 63  
 Houck, J. C., & Denicola, L. A. 2000, *adass IX*, **216**, 591  
 Kalberla, P. M. W., Burton, W. B., Hartmann, D., et al. 2005, *A&A*, **440**, 775  
 Kamble, A., Soderberg, A., Margutti, R., Parrent, J., & Milisavljevic, D. 2014, *ATel*, **6712**, 1  
 Karachentsev, I. D., & Kaisina, E. I. 2013, *AJ*, **146**, 46  
 Li, W., Leaman, J., Chornock, R., et al. 2011, *MNRAS*, **412**, 1441  
 Lipunov, V., Kornilov, V., Gorbvskoy, E., et al. 2010, *AdAst*, **2010**, 349171  
 Margutti, R., Brown, P. J., Kamble, A., et al. 2014, *ATel*, **6719**, 1  
 McMullin, J. P., Waters, B., Schiebel, D., Young, W., & Golap, K. 2007, in *ASP Conf. Ser. 376, Astronomical Data Analysis Software and Systems XVI*, ed. R. A. Shaw, F. Hill, & D. J. Bell (San Francisco, CA: ASP), **127**  
 Mukai, K. 1993, *Legacy*, **3**, 21  
 Podsiadlowski, P., Joss, P. C., & Hsu, J. J. L. 1992, *ApJ*, **391**, 246  
 Prasad, J., & Chengalur, J. 2012, *ExA*, **33**, 157  
 Shappee, B. J., Prieto, J. L., Grupe, D., et al. 2014, *ApJ*, **788**, 48  
 Singh, M., Misra, K., Sahu, D. K., et al. 2019, *MNRAS*, **485**, 5438  
 Smartt, S. J. 2009, *ARA&A*, **47**, 63  
 Smith, N., Li, W., Filippenko, A. V., & Chornock, R. 2011, *MNRAS*, **412**, 1522  
 Soderberg, A. M. 2007, in *AIP Conf. 937, Supernova 1987A: 20 Years After: Supernovae and Gamma-Ray Bursters (Melville, NY: AIP)*, **492**  
 Soderberg, A. M., Chevalier, R. A., Kulkarni, S. R., & Frail, D. A. 2006, *ApJ*, **651**, 1005  
 Soderberg, A. M., Gal-Yam, A., & Kulkarni, S. R. 2004, *GCN*, **2586**, 1  
 Soderberg, A. M., Kulkarni, S. R., Berger, E., et al. 2005, *ApJ*, **621**, 908  
 Srivastav, S., Sahu, D. K., & Anupama, G. C. 2014, *ATel*, **6639**, 1  
 Stockdale, C. J., Kaster, B., Sjouwerman, L. O., et al. 2005, *IAUC*, **8472**, 4  
 Taddia, F., Sollerman, J., Leloudas, G., et al. 2015, *A&A*, **574**, A60  
 Taddia, F., Stritzinger, M. D., Bersten, M., et al. 2018, *A&A*, **609**, A136  
 Terreran, G., Miluzio, M., Ochner, P., et al. 2014, *ATel*, **6640**, 1  
 Tody, D. 1986, *Proc. SPIE*, **627**, 733  
 Tody, D. 1993, *adass II*, **52**, 173  
 Tsvetkov, D. Y., Pavlyuk, N., Lipunov, V., Gorbvskoy, E., & Krushinsky, V. V. 2017, *PZ*, **37**, 2  
 van Marle, A. J., Smith, N., Owocki, S. P., & van Veelen, B. 2010, *MNRAS*, **407**, 2305  
 Vinko, J., Pooley, D., Silverman, J. M., et al. 2017, *ApJ*, **837**, 62  
 Weiler, K. W., Panagia, N., Montes, M. J., & Sramek, R. A. 2002, *ARA&A*, **40**, 387  
 Weiler, K. W., Panagia, N., Stockdale, C., et al. 2011, *ApJ*, **740**, 79  
 White, R. L., Becker, R. H., Helfand, D. J., & Gregg, M. D. 1997, *ApJ*, **475**, 479  
 Woosley, S. E., Heger, A., & Weaver, T. A. 2002, *RvMP*, **74**, 1015